

Jet Properties from Dihadron Correlations in p+p Collisions at $\sqrt{s} = 200$ GeV

S.S. Adler,⁵ S. Afanasiev,²⁰ C. Aidala,¹⁰ N.N. Ajitanand,⁴⁴ Y. Akiba,^{21,40} A. Al-Jamel,³⁵ J. Alexander,⁴⁴ K. Aoki,²⁵ L. Aphecetche,⁴⁶ R. Armendariz,³⁵ S.H. Aronson,⁵ R. Averbeck,⁴⁵ T.C. Awes,³⁶ V. Babintsev,¹⁷ A. Baldisseri,¹¹ K.N. Barish,⁶ P.D. Barnes,²⁸ B. Bassalleck,³⁴ S. Bathe,^{6,31} S. Batsouli,¹⁰ V. Baublis,³⁹ F. Bauer,⁶ A. Bazilevsky,^{5,41} S. Belikov,^{19,17} M.T. Bjorndal,¹⁰ J.G. Boissevain,²⁸ H. Borel,¹¹ M.L. Brooks,²⁸ D.S. Brown,³⁵ N. Bruner,³⁴ D. Bucher,³¹ H. Buesching,^{5,31} V. Bumazhnov,¹⁷ G. Bunce,^{5,41} J.M. Burward-Hoy,^{28,27} S. Butsyk,⁴⁵ X. Camard,⁴⁶ P. Chand,⁴ W.C. Chang,² S. Chernichenko,¹⁷ C.Y. Chi,¹⁰ J. Chiba,²¹ M. Chiu,¹⁰ I.J. Choi,⁵³ R.K. Choudhury,⁴ T. Chujo,⁵ V. Cianciolo,³⁶ Y. Cobigo,¹¹ B.A. Cole,¹⁰ M.P. Comets,³⁷ P. Constantin,¹⁹ M. Csanád,¹³ T. Csörgő,²² J.P. Cussonneau,⁴⁶ D. d'Enterria,¹⁰ K. Das,¹⁴ G. David,⁵ F. Deák,¹³ H. Delagrange,⁴⁶ A. Denisov,¹⁷ A. Deshpande,⁴¹ E.J. Desmond,⁵ A. Devismes,⁴⁵ O. Dietzsch,⁴² J.L. Drachenberg,¹ O. Drapier,²⁶ A. Drees,⁴⁵ A. Durum,¹⁷ D. Dutta,⁴ V. Dzhordzhadze,⁴⁷ Y.V. Efremenko,³⁶ H. En'yo,^{40,41} B. Espagnon,³⁷ S. Esumi,⁴⁹ D.E. Fields,^{34,41} C. Finck,⁴⁶ F. Fleuret,²⁶ S.L. Fokin,²⁴ B.D. Fox,⁴¹ Z. Fraenkel,⁵² J.E. Frantz,¹⁰ A. Franz,⁵ A.D. Frawley,¹⁴ Y. Fukao,^{25,40,41} S.-Y. Fung,⁶ S. Gadrat,²⁹ M. Germain,⁴⁶ A. Glenn,⁴⁷ M. Gonin,²⁶ J. Gosset,¹¹ Y. Goto,^{40,41} R. Granier de Cassagnac,²⁶ N. Grau,¹⁹ S.V. Greene,⁵⁰ M. Grosse Perdekamp,^{18,41} H.-Å. Gustafsson,³⁰ T. Hachiya,¹⁶ J.S. Haggerty,⁵ H. Hamagaki,⁸ A.G. Hansen,²⁸ E.P. Hartouni,²⁷ M. Harvey,⁵ K. Hasuko,⁴⁰ R. Hayano,⁸ X. He,¹⁵ M. Heffner,²⁷ T.K. Hemmick,⁴⁵ J.M. Heuser,⁴⁰ P. Hidas,²² H. Hiejima,¹⁸ J.C. Hill,¹⁹ R. Hobbs,³⁴ W. Holzmann,⁴⁴ K. Homma,¹⁶ B. Hong,²³ A. Hoover,³⁵ T. Horaguchi,^{40,41,48} T. Ichihara,^{40,41} V.V. Ikonnikov,²⁴ K. Imai,^{25,40} M. Inaba,⁴⁹ M. Inuzuka,⁸ D. Isenhower,¹ L. Isenhower,¹ M. Ishihara,⁴⁰ M. Issah,⁴⁴ A. Isupov,²⁰ B.V. Jacak,⁴⁵ J. Jia,⁴⁵ O. Jinnouchi,^{40,41} B.M. Johnson,⁵ S.C. Johnson,²⁷ K.S. Joo,³² D. Jouan,³⁷ F. Kajihara,⁸ S. Kametani,^{8,51} N. Kamihara,^{40,48} M. Kaneta,⁴¹ J.H. Kang,⁵³ K. Katou,⁵¹ T. Kawabata,⁸ A.V. Kazantsev,²⁴ S. Kelly,^{9,10} B. Khachaturov,⁵² A. Khanzadeev,³⁹ J. Kikuchi,⁵¹ D.J. Kim,⁵³ E. Kim,⁴³ G.-B. Kim,²⁶ H.J. Kim,⁵³ E. Kinney,⁹ A. Kiss,¹³ E. Kistenev,⁵ A. Kiyomichi,⁴⁰ C. Klein-Boesing,³¹ H. Kobayashi,⁴¹ L. Kochenda,³⁹ V. Kochetkov,¹⁷ R. Kohara,¹⁶ B. Komkov,³⁹ M. Konno,⁴⁹ D. Kotchetkov,⁶ A. Kozlov,⁵² P.J. Kroon,⁵ C.H. Kuberg,^{1,*} G.J. Kunde,²⁸ K. Kurita,⁴⁰ M.J. Kweon,²³ Y. Kwon,⁵³ G.S. Kyle,³⁵ R. Lacey,⁴⁴ J.G. Lajoie,¹⁹ Y. Le Bornec,³⁷ A. Lebedev,^{19,24} S. Leckey,⁴⁵ D.M. Lee,²⁸ M.J. Leitch,²⁸ M.A.L. Leite,⁴² X.H. Li,⁶ H. Lim,⁴³ A. Litvinenko,²⁰ M.X. Liu,²⁸ C.F. Maguire,⁵⁰ Y.I. Makdisi,⁵ A. Malakhov,²⁰ V.I. Manko,²⁴ Y. Mao,^{38,40} G. Martinez,⁴⁶ H. Masui,⁴⁹ F. Matathias,⁴⁵ T. Matsumoto,^{8,51} M.C. McCain,¹ P.L. McGaughey,²⁸ Y. Miake,⁴⁹ T.E. Miller,⁵⁰ A. Milov,⁴⁵ S. Mioduszewski,⁵ G.C. Mishra,¹⁵ J.T. Mitchell,⁵ A.K. Mohanty,⁴ D.P. Morrison,⁵ J.M. Moss,²⁸ D. Mukhopadhyay,⁵² M. Muniruzzaman,⁶ S. Nagamiya,²¹ J.L. Nagle,^{9,10} T. Nakamura,¹⁶ J. Newby,⁴⁷ A.S. Nyanin,²⁴ J. Nystrand,³⁰ E. O'Brien,⁵ C.A. Ogilvie,¹⁹ H. Ohnishi,⁴⁰ I.D. Ojha,^{3,50} H. Okada,^{25,40} K. Okada,^{40,41} A. Oskarsson,³⁰ I. Otterlund,³⁰ K. Oyama,⁸ K. Ozawa,⁸ D. Pal,⁵² A.P.T. Palounek,²⁸ V. Pantuev,⁴⁵ V. Papavassiliou,³⁵ J. Park,⁴³ W.J. Park,²³ S.F. Pate,³⁵ H. Pei,¹⁹ V. Penev,²⁰ J.-C. Peng,¹⁸ H. Pereira,¹¹ V. Peresedov,²⁰ A. Pierson,³⁴ C. Pinkenburg,⁵ R.P. Pisani,⁵ M.L. Purschke,⁵ A.K. Purwar,⁴⁵ J.M. Qualls,¹ J. Rak,¹⁹ I. Ravinovich,⁵² K.F. Read,^{36,47} M. Reuter,⁴⁵ K. Reygers,³¹ V. Riabov,³⁹ Y. Riabov,³⁹ G. Roche,²⁹ A. Romana,^{26,*} M. Rosati,¹⁹ S.S.E. Rosendahl,³⁰ P. Rosnet,²⁹ V.L. Rykov,⁴⁰ S.S. Ryu,⁵³ N. Saito,^{25,40,41} T. Sakaguchi,^{8,51} S. Sakai,⁴⁹ V. Samsonov,³⁹ L. Sanfratello,³⁴ R. Santo,³¹ H.D. Sato,^{25,40} S. Sato,^{5,49} S. Sawada,²¹ Y. Schutz,⁴⁶ V. Semenov,¹⁷ R. Seto,⁶ T.K. Shea,⁵ I. Shein,¹⁷ T.-A. Shibata,^{40,48} K. Shigaki,¹⁶ M. Shimomura,⁴⁹ A. Sickles,⁴⁵ C.L. Silva,⁴² D. Silvermyr,²⁸ K.S. Sim,²³ A. Soldatov,¹⁷ R.A. Soltz,²⁷ W.E. Sondheim,²⁸ S.P. Sorensen,⁴⁷ I.V. Sourikova,⁵ F. Staley,¹¹ P.W. Stankus,³⁶ E. Stenlund,³⁰ M. Stepanov,³⁵ A. Ster,²² S.P. Stoll,⁵ T. Sugitate,¹⁶ J.P. Sullivan,²⁸ S. Takagi,⁴⁹ E.M. Takagui,⁴² A. Taketani,^{40,41} K.H. Tanaka,²¹ Y. Tanaka,³³ K. Tanida,⁴⁰ M.J. Tannenbaum,⁵ A. Taranenko,⁴⁴ P. Tarján,¹² T.L. Thomas,³⁴ M. Togawa,^{25,40} J. Tojo,⁴⁰ H. Torii,^{25,41} R.S. Towell,¹ V-N. Tram,²⁶ I. Tserruya,⁵² Y. Tsuchimoto,¹⁶ H. Tydesjö,³⁰ N. Tyurin,¹⁷ T.J. Uam,³² H.W. van Hecke,²⁸ J. Velkovska,⁵ M. Velkovsky,⁴⁵ V. Veszprémi,¹² A.A. Vinogradov,²⁴ M.A. Volkov,²⁴ E. Vznuzdaev,³⁹ X.R. Wang,¹⁵ Y. Watanabe,^{40,41} S.N. White,⁵ N. Willis,³⁷ F.K. Wohn,¹⁹ C.L. Woody,⁵ W. Xie,⁶ A. Yanovich,¹⁷ S. Yokkaichi,^{40,41} G.R. Young,³⁶ I.E. Yushmanov,²⁴ W.A. Zajc,^{10,†} C. Zhang,¹⁰ S. Zhou,⁷ J. Zimányi,²² L. Zolin,²⁰ and X. Zong¹⁹

(PHENIX Collaboration)

¹Abilene Christian University, Abilene, TX 79699, U.S.

²Institute of Physics, Academia Sinica, Taipei 11529, Taiwan

³Department of Physics, Banaras Hindu University, Varanasi 221005, India

⁴Bhabha Atomic Research Centre, Bombay 400 085, India

⁵Brookhaven National Laboratory, Upton, NY 11973-5000, U.S.

⁶University of California - Riverside, Riverside, CA 92521, U.S.

- ⁷China Institute of Atomic Energy (CIAE), Beijing, People's Republic of China
- ⁸Center for Nuclear Study, Graduate School of Science, University of Tokyo, 7-3-1 Hongo, Bunkyo, Tokyo 113-0033, Japan
- ⁹University of Colorado, Boulder, CO 80309, U.S.
- ¹⁰Columbia University, New York, NY 10027 and Nevis Laboratories, Irvington, NY 10533, U.S.
- ¹¹Dapnia, CEA Saclay, F-91191, Gif-sur-Yvette, France
- ¹²Debrecen University, H-4010 Debrecen, Egyetem tér 1, Hungary
- ¹³ELTE, Eötvös Loránd University, H - 1117 Budapest, Pázmány P. s. 1/A, Hungary
- ¹⁴Florida State University, Tallahassee, FL 32306, U.S.
- ¹⁵Georgia State University, Atlanta, GA 30303, U.S.
- ¹⁶Hiroshima University, Kagamiyama, Higashi-Hiroshima 739-8526, Japan
- ¹⁷IHEP Protvino, State Research Center of Russian Federation, Institute for High Energy Physics, Protvino, 142281, Russia
- ¹⁸University of Illinois at Urbana-Champaign, Urbana, IL 61801, U.S.
- ¹⁹Iowa State University, Ames, IA 50011, U.S.
- ²⁰Joint Institute for Nuclear Research, 141980 Dubna, Moscow Region, Russia
- ²¹KEK, High Energy Accelerator Research Organization, Tsukuba, Ibaraki 305-0801, Japan
- ²²KFKI Research Institute for Particle and Nuclear Physics of the Hungarian Academy of Sciences (MTA KFKI RMKI), H-1525 Budapest 114, POBox 49, Budapest, Hungary
- ²³Korea University, Seoul, 136-701, Korea
- ²⁴Russian Research Center "Kurchatov Institute", Moscow, Russia
- ²⁵Kyoto University, Kyoto 606-8502, Japan
- ²⁶Laboratoire Leprince-Ringuet, Ecole Polytechnique, CNRS-IN2P3, Route de Saclay, F-91128, Palaiseau, France
- ²⁷Lawrence Livermore National Laboratory, Livermore, CA 94550, U.S.
- ²⁸Los Alamos National Laboratory, Los Alamos, NM 87545, U.S.
- ²⁹LPC, Université Blaise Pascal, CNRS-IN2P3, Clermont-Fd, 63177 Aubiere Cedex, France
- ³⁰Department of Physics, Lund University, Box 118, SE-221 00 Lund, Sweden
- ³¹Institut für Kernphysik, University of Muenster, D-48149 Muenster, Germany
- ³²Myongji University, Yongin, Kyonggido 449-728, Korea
- ³³Nagasaki Institute of Applied Science, Nagasaki-shi, Nagasaki 851-0193, Japan
- ³⁴University of New Mexico, Albuquerque, NM 87131, U.S.
- ³⁵New Mexico State University, Las Cruces, NM 88003, U.S.
- ³⁶Oak Ridge National Laboratory, Oak Ridge, TN 37831, U.S.
- ³⁷IPN-Orsay, Université Paris Sud, CNRS-IN2P3, BP1, F-91406, Orsay, France
- ³⁸Peking University, Beijing, People's Republic of China
- ³⁹PNPI, Petersburg Nuclear Physics Institute, Gatchina, Leningrad region, 188300, Russia
- ⁴⁰RIKEN (The Institute of Physical and Chemical Research), Wako, Saitama 351-0198, JAPAN
- ⁴¹RIKEN BNL Research Center, Brookhaven National Laboratory, Upton, NY 11973-5000, U.S.
- ⁴²Universidade de São Paulo, Instituto de Física, Caixa Postal 66318, São Paulo CEP05315-970, Brazil
- ⁴³System Electronics Laboratory, Seoul National University, Seoul, South Korea
- ⁴⁴Chemistry Department, Stony Brook University, SUNY, Stony Brook, NY 11794-3400, U.S.
- ⁴⁵Department of Physics and Astronomy, Stony Brook University, SUNY, Stony Brook, NY 11794, U.S.
- ⁴⁶SUBATECH (Ecole des Mines de Nantes, CNRS-IN2P3, Université de Nantes) BP 20722 - 44307, Nantes, France
- ⁴⁷University of Tennessee, Knoxville, TN 37996, U.S.
- ⁴⁸Department of Physics, Tokyo Institute of Technology, Oh-okayama, Meguro, Tokyo 152-8551, Japan
- ⁴⁹Institute of Physics, University of Tsukuba, Tsukuba, Ibaraki 305, Japan
- ⁵⁰Vanderbilt University, Nashville, TN 37235, U.S.
- ⁵¹Waseda University, Advanced Research Institute for Science and Engineering, 17 Kikui-cho, Shinjuku-ku, Tokyo 162-0044, Japan
- ⁵²Weizmann Institute, Rehovot 76100, Israel
- ⁵³Yonsei University, IPAP, Seoul 120-749, Korea

The properties of jets produced in $p+p$ collisions at $\sqrt{s}=200$ GeV are measured using the method of two particle correlations. The trigger particle is a leading particle from a large transverse momentum jet while the associated particle comes from either the same jet or the away-side jet. Analysis of the angular width of the near-side peak in the correlation function determines the jet fragmentation transverse momentum j_T . The extracted value, $\sqrt{\langle j_T^2 \rangle} = 585 \pm 6(\text{stat}) \pm 15(\text{sys})$ MeV/c, is constant with respect to the trigger particle transverse momentum, and comparable to the previous lower \sqrt{s} measurements. The width of the away-side peak is shown to be a convolution of j_T with the fragmentation variable, z , and the partonic transverse momentum, k_T . The $\langle z \rangle$ is determined through a combined analysis of the measured π^0 inclusive and associated spectra using jet fragmentation functions measured in e^+e^- collisions. The final extracted values of k_T are then determined to also be independent of the trigger particle transverse momentum, over the range measured, with value of $\sqrt{\langle k_T^2 \rangle} = 2.68 \pm 0.07(\text{stat}) \pm 0.34(\text{sys})$ GeV/c.

I. INTRODUCTION

The goal of this paper is to explore the systematics of jet production and fragmentation in $p + p$ collisions at $\sqrt{s}=200$ GeV by the method of two-particle azimuthal correlations. Knowledge of the jet-fragmentation process is useful not only as a reference measurement for a similar analysis in $Au + Au$ collisions, but can be used as a stringent test of perturbative QCD (pQCD) calculations beyond leading order.

The two-particle azimuthal correlations method worked well at ISR energies ($\sqrt{s}=63$ GeV) and below [1, 2, 3], where it is difficult to directly reconstruct jets, but has not been attempted at higher values of \sqrt{s} . This method is also suitable for jet-analysis in heavy ion data where the large particle multiplicity severely interferes with direct jet reconstruction.

With the beginning of RHIC operation, heavy-ion physics entered a new regime, where pQCD phenomena can be fully explored. High-energy partons materializing into hadronic jets can be used as sensitive probes of the early stage of heavy ion collisions. Measurements carried out during the first three years of RHIC operation at $\sqrt{s_{NN}}=130$ and 200 GeV exhibit many new and interesting features. The high- p_T particle yield was found to be strongly suppressed in $Au + Au$ central collisions [4]. Furthermore, the non-suppression of the high- p_T particle yield in $d + Au$ induced collisions [5] confirmed that the suppression can be fully attributed to the final state interaction of high-energy partons with an extremely opaque nuclear medium formed in $Au+Au$ collisions at RHIC.

Other striking features found in RHIC data are the large asymmetry of particle azimuthal distributions which is attributed to sizable elliptic flow [6, 7] and the observation of the apparent disappearance of the back-to-back jet correlation in central $Au + Au$ collisions [8].

Many of the above mentioned observations can be explained by a large opacity of the medium produced in central $Au + Au$ collisions which causes the scattered partons to lose energy via coherent (Landau-Pomeranchuk-Migdal [9]) gluon bremsstrahlung [10, 11]. It is expected that the medium effect will cause the apparent modification of fundamental properties of hard-scattering like broadening of intrinsic parton transverse momentum k_T [12, 13] and modification of jet fragmentation [14]. Thus the measurement of jet fragmentation properties and intrinsic parton transverse momentum k_T for $p + p$ collisions presented here provides a baseline for comparison to the results in heavy ion collisions, helping to disentangle the complex processes of propagation and possible fragmentation of partons within the excited nuclear medium.

This paper is organized as follows: Section II dis-

cusses the method of two-particle correlations and the relations between jet properties and the angular correlation between parton fragments. The details of the PHENIX experiment relevant to this analysis are outlined in section III. Section IV deals with the analysis of the correlation functions extracted from the $p + p$ data and an evaluation of the $\langle j_T \rangle$ and $\langle k_T \rangle$ quantities. The combined analysis of the inclusive and associated p_T -distributions is discussed in section V and the sensitivity of the associated p_T -distributions to the fragmentation function is discussed in section VI. Section VII presents the resulting values of the partonic transverse momenta k_T corrected for the mean momentum fraction $\langle z_t \rangle$. Section VIII summarizes the results from this paper.

II. JET ANGULAR CORRELATIONS

Jets are produced in the hard scattering of two partons [15, 16, 17, 18]. The overall $p + p$ hard-scattering cross section in “leading logarithm” pQCD is the sum over parton reactions $a + b \rightarrow c + d$ (e.g. $g + q \rightarrow g + q$) at parton-parton center-of-mass (c.m.) energy $\sqrt{\hat{s}}$,

$$\frac{d^3\sigma}{dx_1 dx_2 d\cos\theta^*} = \frac{1}{s} \sum_{ab} f_a(x_1) f_b(x_2) \frac{\pi\alpha_s^2(Q^2)}{2x_1 x_2} \Sigma^{ab}(\cos\theta^*) \quad (1)$$

where $f_a(x_1)$, $f_b(x_2)$, are parton distribution functions, the differential probabilities for partons a and b to carry momentum fractions x_1 and x_2 of their respective partons (e.g. $u(x_2)$), and where θ^* is the scattering angle in the parton-parton c.m. system. The parton-parton c.m. energy squared is $\hat{s} = x_1 x_2 s$, where \sqrt{s} is the c.m. energy of the $p + p$ collision. The parton-parton c.m. system moves with rapidity $y = (1/2) \ln(x_1/x_2)$ in the $p + p$ c.m. system.

Equation 1 gives the p_T spectrum of outgoing parton c (emitted at θ^*), which then fragments into hadrons, e.g. a π^0 . The fragmentation function $D_c^{\pi^0}(z, \mu^2)$ is the probability for a π^0 to carry a fraction $z = p^{\pi^0}/p^c$ of the momentum of outgoing parton c . Equation 1 must be summed over all subprocesses leading to a π^0 in the final state. The parameter μ^2 is an unphysical “factorization” scale introduced to account for collinear singularities in the structure and fragmentation functions [19, 20], which will be ignored for the purposes of this paper.

In this formulation, $f_a(x_1)$, $f_b(x_2)$ and $D_c^{\pi^0}(z)$ represent the “long-distance phenomena” to be determined by experiment; while the characteristic subprocess angular distributions, $\Sigma^{ab}(\cos\theta^*)$, and the coupling constant, $\alpha_s(Q^2) = \frac{12\pi}{25 \ln(Q^2/\Lambda^2)}$, are fundamental predictions of QCD [21, 22, 23] for the short-distance, large- Q^2 , phenomena. The momentum scale $Q^2 \sim p_T^2$ for the scattering subprocess, while $Q^2 \sim \hat{s}$ for a Compton or annihilation subprocess, but the exact meaning of Q^2 tends to be treated as a parameter rather than a

*Deceased

†PHENIX Spokesperson:zajc@nevis.columbia.edu

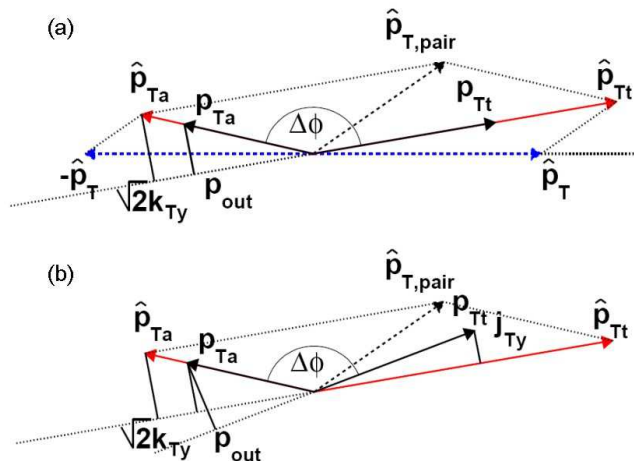


FIG. 1: (color online) (a) Schematic view of a hard scattering event in the plane perpendicular to the beam. Two scattered partons with transverse momenta \hat{p}_T in the partons' center of mass frame are seen in the laboratory frame to have a momenta \hat{p}_{Tt} and \hat{p}_{Ta} . The net pair transverse momentum $\hat{p}_{T, \text{pair}}$ corresponds to the sum of the \vec{k}_T -vectors of the two colliding partons. The trigger and associated jet fragments producing high- p_T particles are labeled as p_{Tt} and p_{Ta} . The projection of \vec{k}_T perpendicular to \hat{p}_{Tt} is labeled as k_{Ty} . The transverse momentum component of the away-side particle \vec{p}_{Ta} perpendicular to trigger particle \vec{p}_{Tt} is labeled as p_{out} . (b) The same schematics as in (a), but the jet fragmentation transverse momentum component j_{Ty} of the trigger jet is also shown.

dynamical quantity.

Figure 1 shows a schematic view of a hard-scattering event. The transverse momentum of the outgoing scattered parton is:

$$p_T = p_T^* = \frac{\sqrt{\hat{s}}}{2} \sin \theta^* \quad . \quad (2)$$

The two scattered partons propagate nearly back-to-back in azimuth from the collision point and fragment into the jet-like spray of final state particles (see Fig. 1(a) where only one fragment of each parton is shown).

It was originally thought that parton collisions were collinear with the $p + p$ collision axis so that the two emerging partons would have the same magnitude of transverse momenta pointing opposite in azimuth. However, it was found [3] that each of the partons carries initial transverse momentum \vec{k}_T , originally described as ‘‘intrinsic’’ [24]. This results in a momentum imbalance (the partons' p_T are not equal) and an acoplanarity (the transverse momentum of one jet does not lie in the plane determined by the transverse momentum of the second jet and the beam axes). The jets are non-collinear having a net transverse momentum $\langle p_T^2 \rangle_{\text{pair}} = 2 \cdot \langle k_T^2 \rangle$.

It is important to emphasize that the $\langle k_T \rangle$ denotes the effective magnitude of the apparent transverse momentum of each colliding parton. The net transverse mo-

mentum of the outgoing parton-pair is $\sqrt{2} \cdot \langle k_T \rangle$. The naive expectation for the pure intrinsic parton transverse momentum based on nucleon constituent quark mass is about $\approx 300 \text{ MeV}/c$ [24, 25]. However, the measurement of net transverse momenta of diphotons, dileptons or dijets over a wide range of center-of-mass energies gives $\langle k_T \rangle$ as large as $5 \text{ GeV}/c$ [26]. It is common to think of the net transverse momentum of a dilepton or dijet pair as composed of 3 components:

$$\frac{\langle p_T^2 \rangle_{\text{pair}}}{2} = \langle k_T^2 \rangle = \langle k_T^2 \rangle_{\text{intrinsic}} + \langle k_T^2 \rangle_{\text{soft}} + \langle k_T^2 \rangle_{\text{NLO}} \quad , \quad (3)$$

where the intrinsic part refers to the possible ‘‘fermi motion’’ of the confined quarks or gluons inside a proton, the NLO part refers to the power law tail at large values of $p_{T, \text{pair}}$ due to the radiation of an initial state or final state hard gluon, which is divergent as the momentum of the radiated gluon goes to zero, and the soft part refers to the actual Gaussian-like distribution observed as $p_{T, \text{pair}} \rightarrow 0$, which is explained by resummation [27].

In the discussion below we will assume that the two components of the vector \vec{k}_T , k_{Tx} and k_{Ty} are Gaussian distributed with equal standard deviations $\sigma_{1\text{parton}, 1d}$, in which case $k_T^2 = k_{Tx}^2 + k_{Ty}^2$ is distributed according to a 2-dimensional (2D) Gaussian [26]. For the net transverse momentum of the jet pair, $\langle p_T^2 \rangle_{\text{pair}} = \sigma_{2\text{partons}, 2d}^2 = 2\sigma_{1\text{parton}, 2d}^2$. Note that the principal difference between the 1 and 2 dimensional Gaussians is that $\langle k_{Tx} \rangle = \langle k_{Ty} \rangle = 0$, while $\langle k_T \rangle \neq 0$ since \vec{k}_T is a 2D radius vector.

The two components of k_T result in different experimentally measurable effects. k_{Ty} leads to the acoplanarity of the dijet pair while k_{Tx} makes the momenta of the jets unequal which results in the smearing of the steeply falling p_T spectrum. This causes the measured inclusive jet or single particle cross section to be larger than the pQCD value given by Eq. 1. This was observed in the original discovery of high p_T particle production at the CERN ISR in 1972 [28] and led to much confusion until the existence and effects of k_T were understood.

Before the advent of QCD, the invariant cross section for the hard-scattering of the electrically charged partons of deeply inelastic scattering was predicted for $p + p$ collisions to follow a general scaling form: [29, 30]

$$E \frac{d^3 \sigma}{d^3 p} = \frac{1}{p_T^n} F(x_T) = \frac{1}{\sqrt{s}^n} G(x_T) \quad , \quad (4)$$

where $x_T = 2p_T/\sqrt{s}$. The cross section has two factors, a function $F(x_T)$ ($G(x_T)$) which ‘scales’, i.e. depends only on the ratio of momenta, and a dimensioned factor, $1/p_T^n$ ($1/\sqrt{s}^n$), where n equals 4 for QED, and for LO-QCD (Eq. 4), analogous to the $1/q^4$ form of Rutherford Scattering. The structure and fragmentation functions are all in the $F(x_T)$ ($G(x_T)$) term. The original high p_T measurements at CERN [28] and Fermilab [31], showed beautiful x_T scaling, but with a value of $n = 8$ instead of $n = 4$, for values of $3 \leq p_T \leq 7 \text{ GeV}/c$. Later

measurements at larger p_T showed the correct scaling in agreement with pQCD and it was realized that the value $n = 8$ at lower values of p_T and \sqrt{s} was produced by the k_{T_x} smearing [16, 17]. More recently, the deviation of π^0 and direct photon inclusive cross sections measurements from pQCD predictions has been used to derive the values of k_T required to bring the measured and smeared pQCD predictions into agreement. [26].

A more direct method to determine k_{T_y} is to measure the acoplanarity of the dijet pair. Such measurements were originally performed at the CERN-ISR using two particle correlations [1, 2, 3, 24]. The same method will be used in the present work.

Hard-scattering in $p+p$ collisions at $\sqrt{s} = 200$ GeV is detected by triggering on a π^0 with transverse momentum $p_{T_i} \geq 3$ GeV/c; and the properties of jets are measured using the method of two particle correlations. The trigger π^0 is a leading particle from a large transverse momentum jet while the associated particle comes from either the same jet or the away-side jet. We will analyze an outgoing dijet pair, with trigger jet transverse momentum magnitude \hat{p}_{T_t} which fragments to a trigger particle with transverse momentum \vec{p}_{T_t} , and an away-side jet transverse momentum magnitude of \hat{p}_{T_a} which fragments to a particle with transverse momentum \vec{p}_{T_a} . The average transverse momentum component of the away-side particle \vec{p}_{T_a} perpendicular to trigger particle \vec{p}_{T_t} in the azimuthal plane is labeled as p_{out} . If the magnitude of the jet transverse fragmentation momentum j_T (Fig. 1(a)) is neglected, the magnitude of $\sqrt{2}k_{T_y}$ can be related to p_{out} : $\sqrt{2}k_{T_y} = p_{out} \hat{p}_{T_a} / p_{T_a} \equiv p_{out} / z_a$. Thus the measurement of p_{out} and the knowledge of the fragmentation variable (z_a) determines the magnitude of the parton's transverse momentum k_T .

The smearing of the steeply falling parton \hat{p}_T spectrum by the k_{T_x} distribution tends to make the trigger jet transverse momentum \hat{p}_{T_t} larger than the away jet transverse momentum \hat{p}_{T_a} . The component of the net transverse momentum of the parton pair along the trigger direction is smeared by $\sqrt{2}k_{T_x}$ such that:

$$\langle (\hat{p}_{T_t} - \hat{p}_{T_{ax}})^2 \rangle = 2 \langle k_{T_x}^2 \rangle = \langle k_T^2 \rangle \quad . \quad (5)$$

For a flat \hat{p}_T spectrum, the smearing would average to zero so that there would be no net shift in the transverse momentum spectrum:

$$\langle \hat{p}_{T_t} - \hat{p}_T \rangle = \langle \hat{p}_T - \hat{p}_{T_{ax}} \rangle = 0 \quad . \quad (6)$$

However, due to the steeply falling \hat{p}_T spectrum, the k_{T_x} smearing results in a net imbalance of the jet-pair towards the trigger direction. In the limit when k_T is collinear with the trigger jet and with the requirement of the Lorentz invariance of \hat{s} ($\hat{p}_T^2 = \hat{p}_{T_t} \hat{p}_{T_a}$) it is easy to see that

$$\langle \hat{p}_{T_t} - \hat{p}_T \rangle = \left\langle \frac{\hat{p}_{T_t}}{\hat{p}_T} (\hat{p}_T - \hat{p}_{T_a}) \right\rangle \simeq \frac{1}{2} \langle \hat{p}_{T_t} - \hat{p}_{T_a} \rangle > 0 \quad . \quad (7)$$

We denote the imbalance of \hat{p}_{T_a} and \hat{p}_{T_t} by the quantity

$$\hat{x}_h = \langle \hat{p}_{T_a} \rangle / \langle \hat{p}_{T_t} \rangle \quad . \quad (8)$$

Jet fragments have a momentum \vec{j}_T perpendicular to the partonic transverse momentum (Fig. 1(b)). This vector is again a two-dimensional vector with one component perpendicular to the jet transverse axis, \vec{p}_T , in the transverse plane and the other component perpendicular to the jet transverse axis in the longitudinal plane (defined by the beam and jet axes). The component of \vec{j}_T projected onto the azimuthal plane is labeled as j_{T_y} . The magnitude of $\langle j_{T_y} \rangle$, the mean value of j_T projected into the plane perpendicular to the jet thrust (see App.A 1), measured at lower energies [1] has been found to be p_T independent and ≈ 400 MeV/c, consistent with measurements in e^+e^- collisions [32, 33].

This analysis uses two-particle azimuthal correlation functions to measure the average relative angles between a trigger π^0 and an associated charged hadron. The angular width of the near- and away-side peak in the correlation function is used to extract the value of $\langle j_T^2 \rangle$ and $\hat{x}_h^{-1} \langle z_t \rangle \sqrt{\langle k_T^2 \rangle}$. An analysis of the associated yields is used to extract the fragmentation function which provides the $\langle z_t \rangle$ and $\langle z_a \rangle$ values used for $\langle k_T^2 \rangle$ extraction. The details on the PHENIX experiment relevant to this analysis follow.

III. EXPERIMENTAL DETAILS

The PHENIX experiment consists of four spectrometer arms - two around mid-rapidity (the central arms) and two at forward rapidity (the muon arms) - along with a set of global detectors. The layout of the PHENIX experiment during RHIC Run-3 is shown in Fig. 2.

Each central arm covers the pseudorapidity range $|\eta| < 0.35$ and 90 degrees in azimuthal angle ϕ . In each of the central arms, charged particles are tracked by a drift chamber (DC) positioned from 2.0 to 2.4m radially outward from the beam axis and 2 or 3 layers of pixel pad chambers (PC1, PC2, PC3 located at 2.4m, 4.2m, 5m in the radial direction, respectively). Particle identification is provided by ring imaging Čerenkov counters (RICH), a time of flight scintillator wall (TOF), and two types of electromagnetic calorimeters (EM-Cal), lead scintillator (PbSc) and lead glass (PbGl). The magnetic field for the central arm spectrometers is axially symmetric around the beam axis. Its component parallel to the beam axis has an approximately Gaussian dependence on the radial distance from the beam axis, dropping from 0.48 T at the center to 0.096 T (0.048 T) at the inner (outer) radius of the DC. A pair of Zero-Degree Calorimeters (ZDC) and a pair of Beam-Beam Counters (BBC) were used for global event characterization. Further details about the design and performance of PHENIX can be found in [34, 35, 36].

A $p+p$ data sample corresponding to an integrated luminosity 0.35 pb^{-1} at $\sqrt{s} = 200$ GeV has been used for the present analysis. It contains a minimum bias (MB) sample of 121M events and a high- p_T triggered sample of 50M events. The MB trigger is obtained

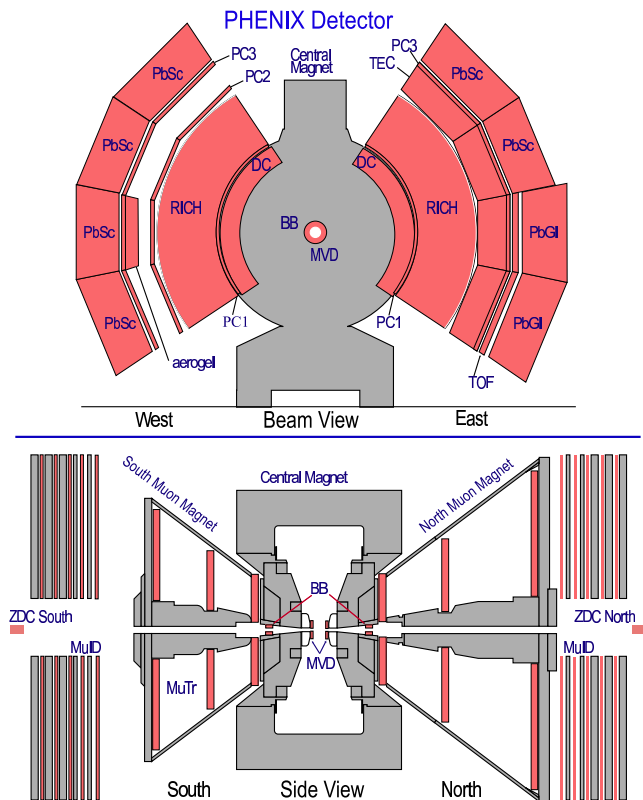


FIG. 2: (color online) The PHENIX experimental layout for the Au+Au run in 2003. The top panel shows the PHENIX central arm spectrometers viewed along the beam axis. The bottom panel shows a side view of the PHENIX muon arm spectrometers and the position of the global detectors (BBC and ZDC).

from the charge multiplicity in the two BBCs situated at large pseudo-rapidity ($\eta \approx \pm(3.0 - 3.9)$). The BBCs were also used to determine the collision vertex, which is limited to a ± 30 cm range in this analysis. The high- p_T trigger requests an additional discrimination on sums of the analog signals from non-overlapping, 2×2 groups of adjacent EMCAL towers situated at mid-rapidity ($|\eta| < 0.35$) equivalent to an energy deposition of 750 MeV [37]. The analysis has been performed separately on the two data sets and no trigger selection bias was found within the quoted errors.

Neutral pions, which are used as trigger particles, are detected by the reconstruction of their $\gamma\gamma$ decay channel. Photons are detected in the EMCAL, which has a timing resolution of ≈ 100 ps (PbSc) and ≈ 300 ps (PbGl) and energy resolution of $\sigma_E/E = 1.9\% \oplus 8.2\%/\sqrt{E(\text{GeV})}$ (PbSc) and $\sigma_E/E = 0.8\% \oplus 8.4\%/\sqrt{E(\text{GeV})}$ (PbGl). In order to improve the signal/background ratio we require the minimum hit energy > 0.3 GeV, a shower profile cut as described in [38], and no accompanying hit in the RICH detector, which serves as a veto for conversion electrons. A sample of the invariant mass distribution of photon pairs detected in the EMCAL is shown in Fig. 3.

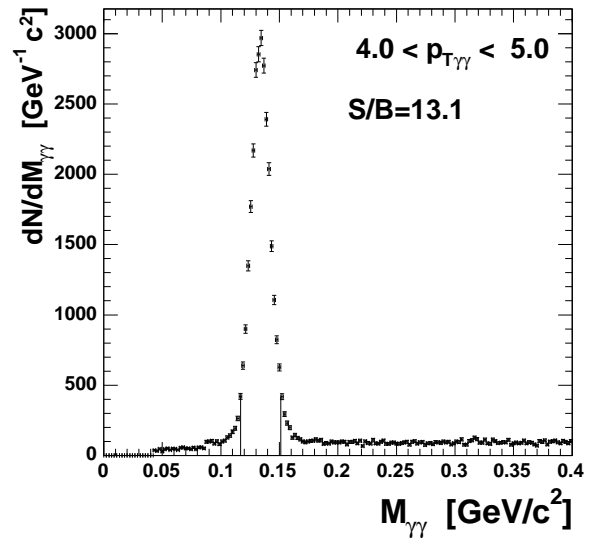


FIG. 3: The measured $\gamma\gamma$ invariant mass distribution for pair p_T in $4 < p_{T,\gamma\gamma} < 5$ GeV/c. The peak is fitted with a Gaussian. The signal/background ratio within 2σ of the mean ranges from ≈ 6 at p_T of 3 GeV/c up to ≈ 15 at 8 GeV/c.

Charged particles are reconstructed in each PHENIX central arm using a drift chamber, followed by two layers of multiwire proportional chambers with pad readout [34]. Particle momenta are measured with a resolution $\delta p/p = 0.7\% \oplus 1.1\%p$ (GeV/c). A confirmation hit is required in PC3. We also require that no signal in the RICH detector is associated with these tracks. These requirements eliminate charged particles which do not originate from the event vertex, such as beam albedo and weak decays, as well as conversion electrons.

High momentum charged pions (above the RICH Čerenkov threshold) are identified using the RICH and EMCAL detectors. Candidate tracks must be associated with a hit in the RICH [39], which corresponds to a minimum momentum of 18 MeV/c for electrons, 3.5 GeV/c for muons, and 4.9 GeV/c for charged pions. In a previous PHENIX publication [40], we have shown that charged particles with reconstructed p_T above 4.9 GeV/c, which have an associated hit in the RICH, are dominantly charged pions and background electrons from photon conversions albedo. The efficiency for detecting charged pions rises quickly past 4.9 GeV/c, reaching an efficiency of $> 90\%$ at $p_T > 6$ GeV/c.

To reject the electron background in the charged pion candidates, the shower information at the EMCAL is used. Since most of the background electrons are genuine low p_T particles that were mis-reconstructed as high p_T particles, simply requiring a large deposition of shower energy in the EMCAL is effective in suppressing the electron background. In this analysis, a momentum-

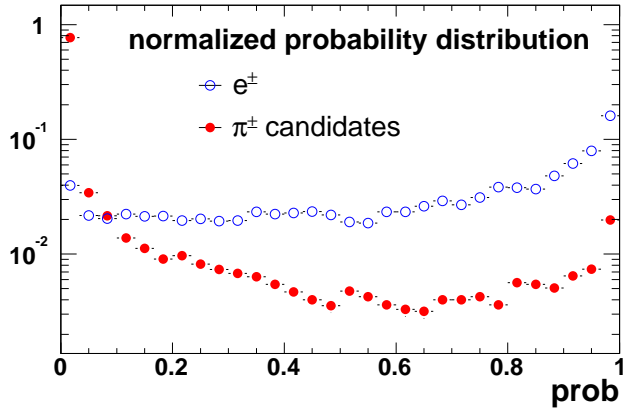


FIG. 4: (color online) The probability distribution for charged pion candidates and electrons derived from the EM shower shape using identified electrons and pions. The integrals have been normalized to one.

dependent energy cut on the EMCal is applied

$$E > 0.3 + 0.15p_T. \quad (9)$$

In addition to this energy cut, the shower shape information [38] is used to further separate the broad hadronic showers from the narrow electromagnetic showers and hence reduce the conversion backgrounds. The difference of the EM shower and hadronic shower is typically characterized by a χ^2 variable [38],

$$\chi^2 = \sum_i \frac{(E_i^{meas} - E_i^{pred})^2}{\sigma_i^2}, \quad (10)$$

where E_i^{meas} is the energy measured at tower i and E_i^{pred} is the predicted energy for an electromagnetic particle of total energy $\sum_i E_i^{meas}$.

In this analysis we use the probability calculated from this χ^2 value for an EM shower, ranging from 0 to 1 with a flat distribution expected for an EM shower, and a peak around 0 for an hadronic shower.

Figure 4 shows the probability distribution for pion and electron candidates, each normalized to one. The pion candidates were required to pass the energy cut and the electrons were selected using particle ID cuts similar to that used in [41]. The electron distribution is relatively flat, while the charged pion distribution peaks at 0. A cut of shower shape probability < 0.2 selects pions above the energy cut with an efficiency of $\gtrsim 80\%$. Detailed knowledge of the pion efficiency is not necessary, since we present in this paper the per-trigger pion conditional-yield distributions, for which this efficiency cancels out.

Since the energy and shower shape cuts are independent of each other, we can fix one cut and then vary the second to check the remaining background level from conversions. The energy cut in Eq. (9) is chosen such that the raw pion yield is found to be insensitive to the variation in the shower shape probability. Figure 5

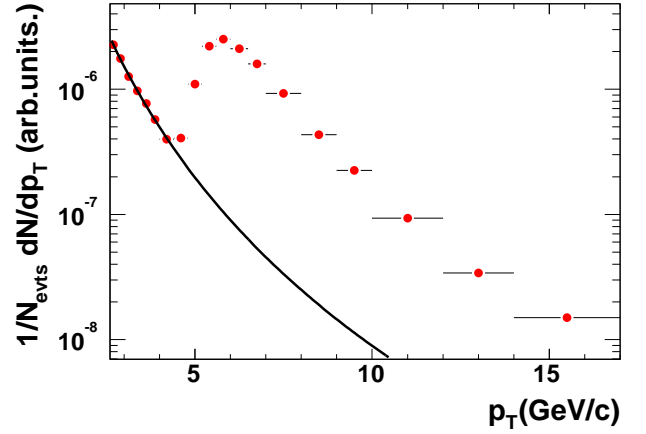


FIG. 5: (color online) The raw charged pion transverse momentum spectrum, with the final cuts applied. The level of the remaining background is estimated from an extrapolation from low- p_T and is shown as a black line.

shows the raw pion spectra for EMCal-RICH triggered events as a function of p_T , with the above cuts applied. The pion turn on from $4.9 - 7$ GeV/ c is clearly visible. Below p_T of 5 GeV/ c , the remaining background comes mainly from the random association of charged particles with hits in the RICH detector. The background level is less than 5% from 5 – 16 GeV/ c , which is the p_T range for the charged pion data presented in this paper.

IV. CORRELATION FUNCTION

The analysis uses two-particle azimuthal correlation functions between a neutral pion and an associated charged hadron to measure the distribution of the azimuthal angle difference $\Delta\phi = \phi_t - \phi_a$ (see Fig. 6). Whenever a π^0 was found in an event, the real, $dN_{\text{uncorr}}/d\Delta\phi$, and mixed, $dN_{\text{mix}}/d\Delta\phi$, distributions for given p_{Tt} (π^0) and p_{Ta} (charged hadron) were accumulated (left panel of Fig. 6). Mixed events were obtained by randomly selecting each member of a particle pair from different events having similar vertex position. Then the mixed event distribution was used to correct the correlation function for effects of the limited PHENIX azimuthal acceptance and for the detection efficiency, to the extent that it remains constant over the data sample.

We fit the raw $dN_{\text{uncorr}}/d\Delta\phi$ distribution with the product

$$\frac{dN_{\text{uncorr}}}{d\Delta\phi} = \frac{1}{\mathcal{N}} \frac{dN_{\text{mix}}}{d\Delta\phi} \cdot (C_0 + C_1 \cdot f_{\text{near}}(\Delta\phi) + C_2 \cdot f_{\text{away}}(\Delta\phi)) \quad (11)$$

where the mixed event distribution is normalized to 2π ($\mathcal{N} = \sum dN_{\text{mix}}^i/d\Delta\phi$ see blue dashed line on the left panel of Fig. 6), C_{0-2} are constant factors to be determined from the fit, $f_{\text{near}}(\Delta\phi)$ and $f_{\text{away}}(\Delta\phi)$ are the

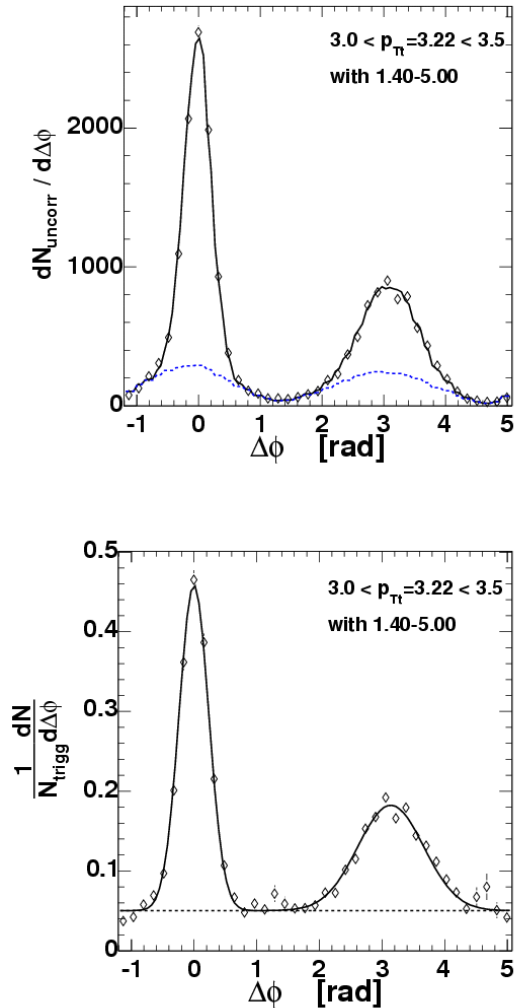


FIG. 6: (color online) An example of the correlation functions for $3 < p_{Tt} < 3.5$ GeV/c and associated particles in $1.4 < p_{Ta} < 5$ GeV/c. (upper) Unnormalized pair-yield distribution plotted with the fit function which is two Gaussians modulated by the pair detection efficiency derived from the mixed distribution (blue dashed line). (lower) Per π^0 trigger yield distribution corrected for the pair detection efficiency. Dashed line represents the constant term in the fit.

near- and away-side peak fit functions respectively. Traditionally, the Gaussian functions, around $\Delta\phi = 0$ and around $\Delta\phi = \pi$, are used for $f_{\text{near}}(\Delta\phi)$ and $f_{\text{away}}(\Delta\phi)$. This leaves a total of five free parameters to be determined - the areas and widths of the above two Gaussians: Y_N , σ_N for the near-angle component and Y_F , σ_A for the away-angle component and the constant term describing an uncorrelated distribution of particle pairs which are not associated with jets. However, the assumption of the Gaussian shape of the angular correlation induced by jet fragmentation is justified only in the high- p_T region where the relative angles are small.

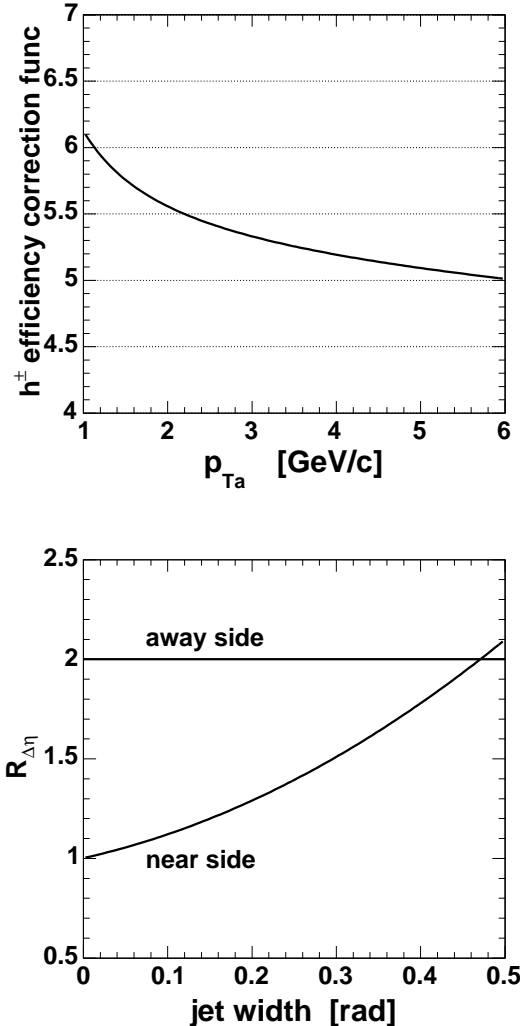


FIG. 7: (upper) Inclusive charged hadron efficiency correction function. (lower) η acceptance correction factor for loss of jet pairs outside the limited η -acceptance of the PHENIX experiment.

In order to access also a lower p_T region we used an alternative parameterization of $f_{\text{near}}(\Delta\phi)$ and $f_{\text{away}}(\Delta\phi)$ which will be discussed later in the text.

The normalized correlation function was constructed as a ratio of real and mixed distributions multiplied by η -acceptance correction factor $R_{\Delta\eta}$, divided by p_T -dependent efficiency correction $\epsilon(p_T)$ (see left panel of Fig. 7) and divided by the number of π^0 triggers.

$$\frac{1}{N_{\text{trigg}}} \frac{dN}{d\Delta\phi} = \frac{R_{\Delta\eta}}{N_{\text{trigg}} \epsilon(p_T)} \frac{dN_{\text{uncorr}}(\Delta\phi)/d\Delta\phi}{dN_{\text{mix}}(\Delta\phi)/d\Delta\phi} \cdot \mathcal{N}. \quad (12)$$

The $R_{\Delta\eta}$ correction factor which accounts for limited η acceptance of the PHENIX experiment (see right panel of Fig. 7) for the the near-side yield, with an assumption that the angular jet width is the same in $\Delta\eta$

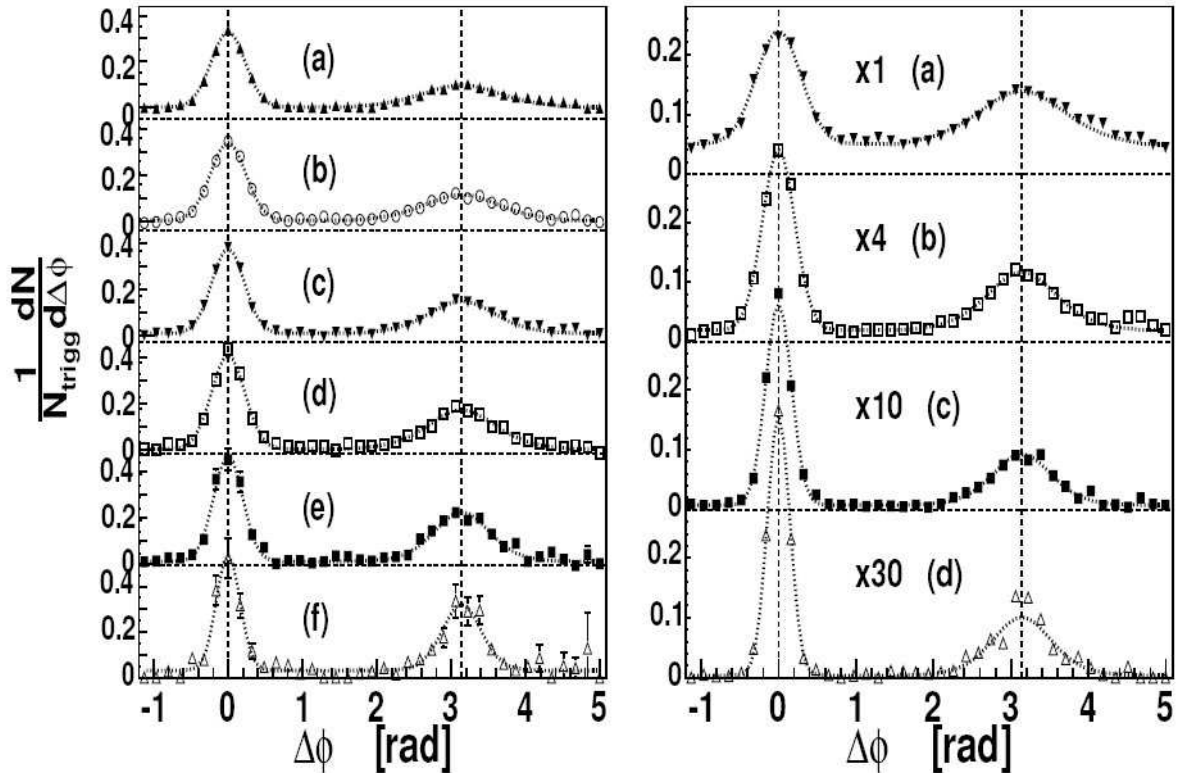


FIG. 8: (left) Measured yield of charged hadrons with away-side transverse momentum $1.4 < p_{T_a} < 5.0$ GeV/c associated with a trigger π^0 of transverse momenta given in in Table I. (right) Measured yield of charged hadrons associated with a trigger π^0 of fixed transverse momentum $3.0 < p_{T_t} < 10.0$ GeV/c and the away-side transverse momenta given in Table I. The dashed lines corresponds to the fit of two Gaussian functions representing the trigger (t) jet and away-side (a) jet correlation. The $\chi^2(\text{DOF})$ σ_N and $\sqrt{\langle p_{\text{out}}^2 \rangle}$ values extracted from these fits are tabulated in Table I.

TABLE I: The $\chi^2(\text{DOF})$ σ_N and $\sqrt{\langle p_{\text{out}}^2 \rangle}$ values extracted for the correlation function shown in Fig. 8. All units in rad and GeV/c. Only the statistical errors are shown.

$1.4 < p_{T_a} < 5.0$ GeV/c				$3.0 < p_{T_t} < 10.0$ GeV/c			
p_{T_t} GeV/c	$\chi^2(\text{DOF}=34)$	σ_N	$\sqrt{\langle p_{\text{out}}^2 \rangle}$	p_{T_a}	$\chi^2(\text{DOF}=34)$	σ_N	$\sqrt{\langle p_{\text{out}}^2 \rangle}$
(a) 2.5 – 3.0	69.4	$0.26 \pm 4\text{E-}03$	1.17 ± 0.07	(a) 1.0 – 2.0	188.4	$0.29 \pm 4\text{E-}03$	0.87 ± 0.03
(b) 3.0 – 3.5	79.6	$0.24 \pm 4\text{E-}03$	1.19 ± 0.05	(b) 2.0 – 3.0	63.2	$0.21 \pm 3\text{E-}03$	1.16 ± 0.04
(c) 3.5 – 4.5	61.2	$0.22 \pm 3\text{E-}03$	1.04 ± 0.04	(c) 3.0 – 4.0	50.3	$0.16 \pm 4\text{E-}03$	1.36 ± 0.06
(d) 4.5 – 5.5	52.7	$0.22 \pm 6\text{E-}03$	1.08 ± 0.06	(d) 4.0 – 5.0	63.2	$0.14 \pm 4\text{E-}03$	1.69 ± 0.13
(e) 5.5 – 6.5	38.4	$0.20 \pm 8\text{E-}03$	0.90 ± 0.06				
(f) 6.5 – 8.0	31.6	$0.16 \pm 1\text{E-}02$	0.64 ± 0.06				

and in $\Delta\phi$, can be written as

$$R_{\Delta\eta} = \frac{1}{\frac{1}{\sqrt{2\pi\sigma_N^2}} \int_{-0.7}^{0.7} \exp\left(-\frac{\Delta\eta}{2\sigma_N^2}\right) \text{acc}(\Delta\eta) d\eta}, \quad (13)$$

where $\text{acc}(\Delta\eta)$ represent the PHENIX pair acceptance function in $|\Delta\eta|$. It can be obtained by convolving two flat distributions in $|\Delta\eta| < 0.35$, so $\text{acc}(\Delta\eta)$ has a simple triangular shape: $\text{acc}(\Delta\eta) = (0.7 - |\Delta\eta|)/0.7$. For the away-side yield the corresponding $R_{\Delta\eta}$ is

$$R_{\Delta\eta} = \frac{2(0.7)}{\frac{1}{\sqrt{2\pi\sigma_N^2}} \int_{-0.7}^{0.7} \text{acc}(\Delta\eta) d\eta} = 2. \quad (14)$$

$R_{\Delta\eta}$ equals 2, because the pair efficiency has a triangular shape in $|\Delta\eta| < 0.7$, which results in 50% average efficiency when the real jet pair distribution is flat in $|\Delta\eta| < 0.7$. Normalized correlation functions for various p_{T_t} and p_{T_a} are shown in Fig. 8.

For two particles with transverse momenta p_{T_t} , p_{T_a} from the same jet, the width of the near-side correlation distribution can be related to the RMS value of the j_T vector component, j_{T_y} , perpendicular to the parton momentum as

$$\sigma_N^2 = \langle \Delta\phi^2 \rangle = \left\langle \left(\frac{j_{T_y}}{p_{T_a}} \right)^2 + \left(\frac{j_{T_y}}{p_{T_t}} \right)^2 \right\rangle, \quad (15)$$

where we assume $\langle j_{Ty}^2 \rangle \ll p_{Tt}^2$ and p_{Ta}^2 and thus the arcsine function can be approximated by its argument and we can solve for ¹

$$\sqrt{\langle j_T^2 \rangle} = \sqrt{2 \langle j_{Ty}^2 \rangle} \simeq \sqrt{2} \frac{p_{Tt} p_{Ta}}{\sqrt{p_{Tt}^2 + p_{Ta}^2}} \sigma_N \quad . \quad (16)$$

In order to extract $\langle |k_{Ty}| \rangle$, or $\langle k_T^2 \rangle$, we start with the relation [1, 24] between the magnitude of p_{out} , (see Fig. 1)

$$p_{out} = p_{Ta} \sin \Delta\phi, \quad (17)$$

which is the transverse momentum component of the away-side particle \vec{p}_{Ta} perpendicular to trigger particle \vec{p}_{Tt} in the azimuthal plane (see Fig. 1), and k_{Ty} :

$$\langle |p_{out}| \rangle^2 = x_E^2 \left[2 \langle |k_{Ty}| \rangle^2 + \langle |j_{Ty}| \rangle^2 \right] + \langle |j_{Ty}| \rangle^2, \quad (18)$$

where

$$x_E = -\frac{\vec{p}_{Tt} \cdot \vec{p}_{Ta}}{p_{Tt}^2} = -\frac{p_{Ta} \cos \Delta\phi}{p_{Tt}} \simeq \frac{z_a \hat{p}_{Ta}}{z_t \hat{p}_{Tt}} \quad (19)$$

represents the fragmentation variable of the away-side jet. [2, 3] We note however, that [24] explicitly neglected $\langle z_t \rangle = \langle p_{Tt} / \hat{p}_{Tt} \rangle$ in the formula at ISR energies, where $\langle z_t \rangle \simeq 0.85$, while it is not negligible at $\sqrt{s}=200$ GeV. Furthermore, as mentioned earlier, the average values of trigger and associated jet momenta are generally not the same. There is a systematic momentum imbalance due to k_T -smearing of the steeply falling parton momentum distribution. The event sample with a condition of $p_{Tt} > p_{Ta}$ is dominated by configurations where the k_T -vector is parallel to the trigger jet and antiparallel to the associated jet and $\langle \hat{p}_{Tt} - \hat{p}_{Ta} \rangle \neq 0$. Here we introduce the hadronic variable x_h in analogy to the partonic variable \hat{x}_h

$$x_h \equiv \frac{p_{Ta}}{p_{Tt}} \quad \hat{x}_h = \hat{x}_h(\langle k_T^2 \rangle, x_h) \equiv \frac{\langle \hat{p}_{Ta} \rangle}{\langle \hat{p}_{Tt} \rangle} \quad (20)$$

The detailed discussion on the magnitude of this imbalance is given later. In order to derive the relation between the magnitude of p_{out} and k_T let us first consider the simple case where we have neglected both trigger and associated $\langle j_T \rangle$ (see panel (a) on Fig. 1). In this case one can see that

$$\begin{aligned} \langle |p_{out}| \rangle |_{j_{Tt}=j_{Ta}=0} &\equiv \langle |p_{out}| \rangle_{00} = \\ &= \sqrt{2} \langle |k_{Ty}| \rangle \frac{p_{Ta}}{\langle \hat{p}_{Ta} \rangle} = \\ &= \sqrt{2} \langle |k_{Ty}| \rangle \langle z_t \rangle \frac{x_h}{\hat{x}_h}. \end{aligned}$$

Rewriting the formula for p_{out} in terms of RMS we get

$$\sqrt{\langle p_{out}^2 \rangle}_{00} = \langle z_t \rangle \sqrt{\langle k_T^2 \rangle} \frac{x_h}{\hat{x}_h} \quad ,$$

where we have taken $\langle k_T^2 \rangle = \langle 2k_{Ty}^2 \rangle$.

However, the jet fragments are produced with finite jet transverse momentum j_T . The situation when the trigger particle is produced with $j_{Tty} > 0$ GeV/c and the associated particle with $j_{Tay} = 0$ GeV/c is shown in Fig. 1b. The p_{out} vector picks up an additional component

$$\begin{aligned} \langle p_{out}^2 \rangle |_{j_{Tt}>0, j_{Ta}=0} &= \\ &= \left[\langle p_{out}^2 \rangle_{00} + \frac{\langle j_{Tty}^2 \rangle}{p_{Tt}^2} (p_{Ta}^2 - \langle p_{out}^2 \rangle_{00}) \right] \frac{p_{Ta}^2 - \langle j_{Tty}^2 \rangle}{p_{Tt}^2} \end{aligned}$$

With an assumption of $j_{Tty} \ll p_{Tt}$ we found that

$$\langle p_{out}^2 \rangle |_{j_{Tt}>0, j_{Ta}=0} = x_h^2 \left[\langle z_t \rangle^2 \langle k_T^2 \rangle \frac{1}{\hat{x}_h^2} + \langle j_{Tty}^2 \rangle \right]$$

We include j_{Ta} in the same approximation, $j_{Tay} \ll p_{Ta}$, i.e. collinearity of j_{Ta} and p_{out} with result

$$\langle p_{out}^2 \rangle = x_h^2 \left[\langle z_t \rangle^2 \langle k_T^2 \rangle \frac{1}{\hat{x}_h^2} + \langle j_{Tty}^2 \rangle \right] + \langle j_{Tay}^2 \rangle \quad (21)$$

and we solve for $\langle z_t \rangle \sqrt{\langle k_T^2 \rangle} / \hat{x}_h$

$$\frac{\langle z_t \rangle \sqrt{\langle k_T^2 \rangle}}{\hat{x}_h} = \frac{1}{x_h} \sqrt{\langle p_{out}^2 \rangle - \langle j_{Tay}^2 \rangle - x_h^2 \langle j_{Tty}^2 \rangle} \quad .$$

If we assume no difference between j_{Tt} and j_{Ta} then we have

$$\frac{\langle z_t(k_T, x_h) \rangle \sqrt{\langle k_T^2 \rangle}}{\hat{x}_h(k_T, x_h)} = \frac{1}{x_h} \sqrt{\langle p_{out}^2 \rangle - \langle j_{Ty}^2 \rangle (1 + x_h^2)} \quad (22)$$

All quantities on the right-hand side of Eq. (22) can be directly extracted from the correlation function. The correlation functions are measured in the variable $\Delta\phi$ in bins of p_{Tt} and p_{Ta} (*e.g.* see Fig. 8), and the rms of the near and away peaks σ_N and σ_A are extracted. We tabulated σ_N and σ_A for many combinations of p_{Tt} and p_{Ta} (see Fig. 9 and Fig. 10).

Initially, we used the approximation $\sqrt{\langle p_{out}^2 \rangle} \sim p_{Ta} \sin \sigma_A$ in Eq. 22. However, we have noticed that this approximation and other approximations for $\sqrt{\langle p_{out}^2 \rangle}$ proposed *e.g.* in reference [42] (see appendix A 2) are inadequate for $\sigma_A > 0.4$ radians, so we don't use σ_A to calculate k_T .

We extract $\sqrt{\langle p_{out}^2 \rangle}$ directly for all values of p_{Tt} p_{Ta} (even for wide bins in p_{Ta} using the $\langle p_{Ta} \rangle$ of the bin) by fitting the correlation function in the $\pi/2 < \Delta\phi < 3\pi/2$ region by

$$\begin{aligned} \frac{dN_{away}}{d\Delta\phi} \Big|_{\pi/2}^{3\pi/2} &= \frac{dN}{dp_{out}} \frac{dp_{out}}{d\Delta\phi} = \\ &= \frac{-p_{Ta} \cos \Delta\phi}{\sqrt{2\pi} \langle p_{out}^2 \rangle \text{Erf}\left(\frac{\sqrt{2} p_{Ta}}{\sqrt{\langle p_{out}^2 \rangle}}\right)} \exp\left(-\frac{p_{Ta}^2 \sin^2 \Delta\phi}{2 \langle p_{out}^2 \rangle}\right) \end{aligned} \quad (23)$$

¹ For relations between $\sqrt{\langle X^2 \rangle}$ and $\langle |X_y| \rangle$, where X is any 2D quantity, see App.A 1

TABLE II: Measured widths of the near- and away-angle $\pi^0 - h^\pm$ correlation peaks for various trigger particle momenta. Only the statistical errors are shown.

$p_{T_t}=3.39$ GeV/c			$p_{T_t}=4.40$ GeV/c			$p_{T_t}=5.41$ GeV/c			$p_{T_t}=6.40$ GeV/c		
p_{T_a}	σ_N rad	σ_A rad	p_{T_a}	σ_N rad	σ_A rad	p_{T_a}	σ_N rad	σ_A rad	p_{T_a}	σ_N rad	σ_A rad
1.59	0.27 ± 0.01	0.58 ± 0.05	1.72	0.28 ± 0.02	0.50 ± 0.03	1.51	0.26 ± 0.01	0.49 ± 0.03	1.34	0.40 ± 0.03	0.68 ± 0.05
1.84	0.24 ± 0.01	0.52 ± 0.03	2.14	0.18 ± 0.01	0.47 ± 0.06	2.22	0.21 ± 0.02	0.39 ± 0.05	1.64	0.30 ± 0.02	0.58 ± 0.05
2.22	0.23 ± 0.01	0.52 ± 0.03	2.53	0.20 ± 0.01	0.47 ± 0.04	2.88	0.17 ± 0.01	0.37 ± 0.05	1.94	0.23 ± 0.02	0.52 ± 0.06
2.73	0.19 ± 0.01	0.46 ± 0.04	3.17	0.16 ± 0.01	0.38 ± 0.04	4.01	0.14 ± 0.02	0.34 ± 0.07	2.29	0.23 ± 0.02	0.40 ± 0.03
3.24	0.19 ± 0.01	0.47 ± 0.04	4.36	0.14 ± 0.01	0.39 ± 0.07				2.74	0.17 ± 0.01	0.41 ± 0.05
3.93	0.17 ± 0.01	0.41 ± 0.03							3.36	0.17 ± 0.02	0.36 ± 0.04
5.04	0.12 ± 0.01	0.38 ± 0.05									

where we assumed a Gaussian distribution in p_{out} . We still use a Gaussian function in $\Delta\phi$ in the near angle peak to extract $\sqrt{\langle j_T^2 \rangle}$. The $\sqrt{\langle p_{out}^2 \rangle}$ values extracted from the fit of the functional form (23) are shown in Fig. 11 and Fig. 12.

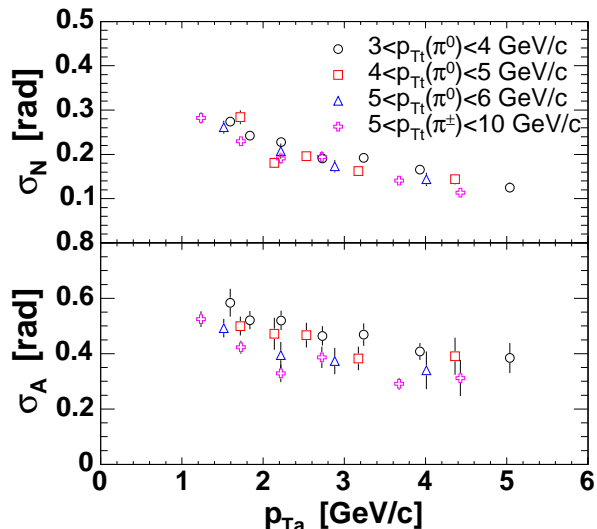


FIG. 9: (color online) (top) The width of the near-side peak σ_N with p_{T_a} for various values of p_{T_t} as indicated in legend. (bottom) The width of the far-side peak σ_A with p_{T_a} for the same p_{T_t} selection.

The per-trigger yields as a function of p_{T_t} for fixed associated $1.4 < p_{T_a} < 5.0$ GeV/c bin are shown in Fig. 13. There is a distinct behavior of the near-side yield which varies with trigger p_{T_t} much less than the away-side yield. For the away-side, this reflects the fact that the particle detected in the fixed associated bin are produced from the lower z region of the fragmentation function for events with higher trigger p_{T_t} . For the near-side jet, this multiplicity increase is reduced due to the fact that with increasing p_{T_t} the near-side jet energy increases; however, at the same time the larger fraction of this energy is taken away by the more energetic trigger particle. Thus the relative change in z is smaller on the near-side.

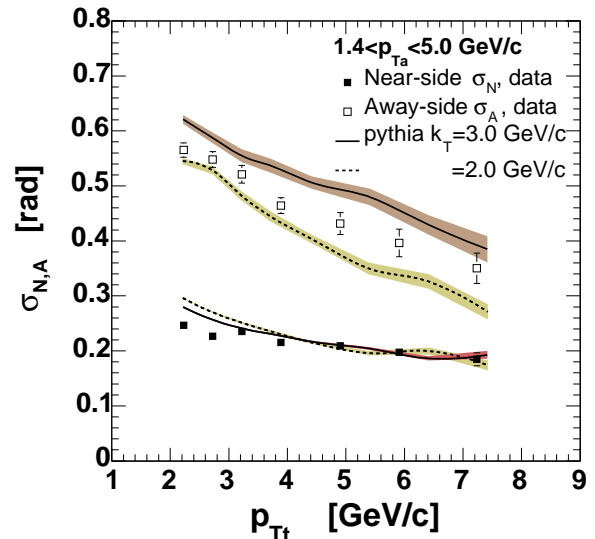


FIG. 10: (color online) The near-side (squares) and away-side (circles) width as a function of trigger- π^0 p_{T_t} . The associated charged particle momenta are in the $1.4 < p_{T_a} < 5.0$ GeV/c region. The curves are from a PYTHIA calculation with the values of k_T indicated. The data values are given in Table III.

TABLE III: The σ_N and σ_A values shown in Fig. 10. All units in rad and GeV/c. Only the statistical errors are shown.

p_{T_t}	σ_N	σ_A
2.23	0.247 ± 0.002	0.565 ± 0.013
2.72	0.227 ± 0.003	0.548 ± 0.014
3.22	0.235 ± 0.004	0.521 ± 0.016
3.89	0.215 ± 0.004	0.464 ± 0.014
4.90	0.210 ± 0.006	0.431 ± 0.020
5.91	0.197 ± 0.009	0.396 ± 0.025
7.23	0.185 ± 0.012	0.350 ± 0.028

In order to extract $\langle z_t \rangle$ and \hat{x}_h knowledge of the fragmentation function is needed; a detailed discussion is given in following sections.

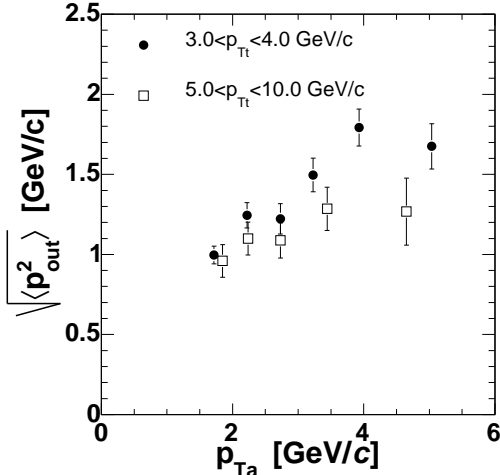


FIG. 11: Extracted values of $\sqrt{\langle p_{out}^2 \rangle}$ for $3.0 < p_{Tt} < 4.0$ and $5.0 < p_{Tt} < 10.0$ GeV/c for various values of p_{Ta} using the direct p_{out} extraction method based on fitting the away-side peak by Eq. (23).

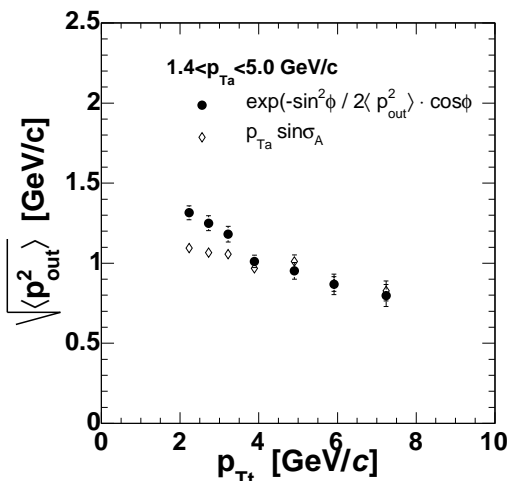


FIG. 12: (solid circles) Extracted values of $\sqrt{\langle p_{out}^2 \rangle}$ for $1.4 < p_{Ta} < 5.0$ GeV/c for various values of p_{Tt} from Eq. (23). (open diamonds) Indirect $p_{out} = p_{Ta} \sin(\sigma_A)$ values.

A. $\sqrt{\langle j_T^2 \rangle}$ and $\hat{x}_h^{-1} \langle z_t \rangle \sqrt{\langle k_T^2 \rangle}$ results

The measurement is performed in two different kinematical regimes; first the transverse momentum of the trigger particle, p_{Tt} , is fixed and the peak width is measured for different values of associated particle transverse momenta p_{Ta} (Fig. 9). (Note that in the region of overlap, the data are in excellent agreement with a

TABLE IV: The $\sqrt{\langle p_{out}^2 \rangle}$ values shown in Fig. 11 and Fig. 12. All units in GeV/c. Only the statistical errors are shown.

	$1.4 < p_{Ta} < 5.0$		$3 < p_{Tt} < 4$		$5 < p_{Tt} < 10$	
p_{Tt}	$\sqrt{\langle p_{out}^2 \rangle}$	p_{Ta}	$\sqrt{\langle p_{out}^2 \rangle}$	p_{Ta}	$\sqrt{\langle p_{out}^2 \rangle}$	p_{Ta}
2.23	1.315 ± 0.043	1.72	0.996 ± 0.056	1.85	0.960 ± 0.102	
2.72	1.250 ± 0.046	2.22	1.244 ± 0.079	2.24	1.100 ± 0.103	
3.22	1.182 ± 0.049	2.73	1.222 ± 0.095	2.73	1.088 ± 0.110	
3.89	1.011 ± 0.038	3.23	1.496 ± 0.105	3.44	1.285 ± 0.136	
4.90	0.953 ± 0.052	3.93	1.793 ± 0.115	4.65	1.268 ± 0.210	
5.91	0.868 ± 0.064	5.04	1.675 ± 0.141			
7.24	0.798 ± 0.068					

TABLE V: The near and away side conditional yield per number of triggers for $1.4 < p_{Ta} < 5.0$ GeV/c shown in Fig. 13. All units in rad and GeV/c. Only the statistical errors are shown.

p_{Tt}	Y_N	Y_A
2.23	1.911 ± 0.018	1.717 ± 0.044
2.72	1.863 ± 0.022	1.908 ± 0.055
3.22	2.032 ± 0.032	2.130 ± 0.071
3.89	1.966 ± 0.033	2.360 ± 0.074
4.90	2.120 ± 0.061	2.611 ± 0.123
5.91	2.153 ± 0.098	2.992 ± 0.196
7.24	2.174 ± 0.125	3.690 ± 0.242

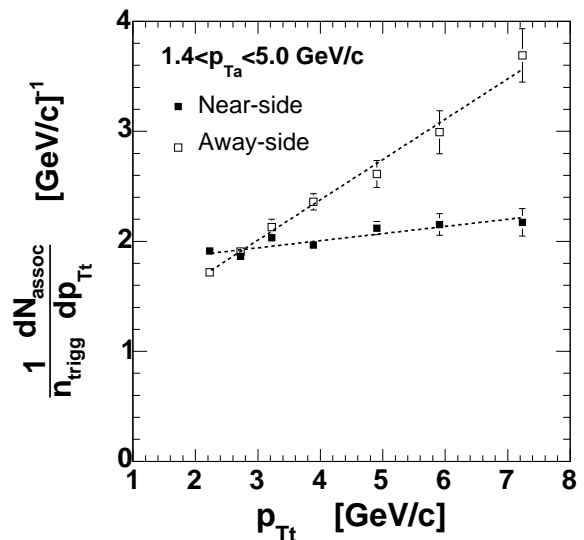


FIG. 13: Measured yield of charged hadrons associated with one trigger π^0 with transverse momenta indicated in Table I and associated charged hadron with $1.4 < p_T < 5.0$ GeV/c. Dashed lines represent the linear fit.

TABLE VI: The $\sqrt{\langle j_T^2 \rangle}$ values shown in Fig. 14 and Fig. 15. All units in rad and GeV/c. Only the statistical errors are shown.

$1.4 < p_{T_a} < 5.0$		$3 < p_{T_t} < 4$	
p_{T_t}	$\sqrt{\langle j_T^2 \rangle}$	p_{T_a}	$\sqrt{\langle j_T^2 \rangle}$
3.22	0.587 ± 0.009	1.72	0.562 ± 0.011
3.89	0.577 ± 0.009	2.22	0.597 ± 0.014
4.90	0.600 ± 0.017	2.73	0.572 ± 0.017
5.91	0.596 ± 0.026	3.23	0.590 ± 0.020
7.24	0.597 ± 0.038	3.93	0.603 ± 0.017
8.34	0.632 ± 0.085	5.04	0.506 ± 0.029
$4 < p_{T_t} < 5$		$5 < p_{T_t} < 6$	
p_{T_a}	$\sqrt{\langle j_T^2 \rangle}$	p_{T_a}	$\sqrt{\langle j_T^2 \rangle}$
1.72	0.643 ± 0.036	1.52	0.529 ± 0.030
2.14	0.492 ± 0.032	2.22	0.581 ± 0.049
2.53	0.608 ± 0.035	2.88	0.590 ± 0.047
3.17	0.590 ± 0.032	4.01	0.603 ± 0.063
4.36	0.631 ± 0.052		

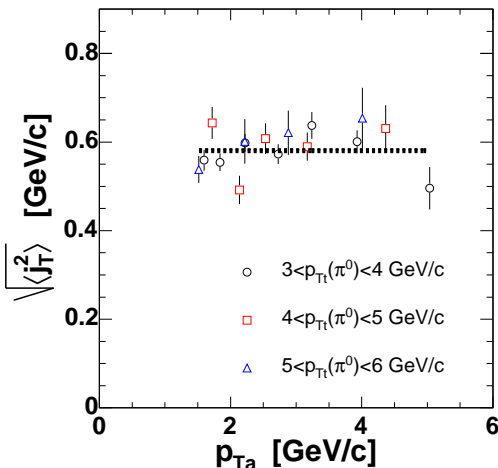


FIG. 14: (color online) $\langle j_T^2 \rangle$ values calculated according Eq. (16). The dashed line represents the 0th-order polynomial fit in the $1.5 < p_{T_a} < 5$ GeV/c region.

previous measurement [43].) In the second case, particle pairs with a fixed associated bin $1.4 < p_{T_a} < 5.0$ GeV/c and various p_{T_t} are selected (Fig. 10). It is evident that both near and away-side correlation peaks in all cases reveal a decreasing trend with p_{T_a} and p_{T_t} .

However, the asymptotic behavior of σ_N and σ_A is different. Whereas the magnitude of σ_N , according to Eq. (16), should vanish for large values of p_{T_t} and p_{T_a} , the σ_A according to Eq. (22) should be approximately constant around $\hat{x}_h^{-1}(z_t) \sqrt{\langle k_T^2 \rangle} / p_{T_t}$ for large values of p_{T_a} . The $\langle z_t \rangle$ and \hat{x}_h quantities are implicitly p_{T_a} dependent, however, their ratio is roughly ~ 1 so that the asymptotic value of $\sigma_A|_{p_{T_a} \rightarrow \infty} \sim \sqrt{\langle k_T^2 \rangle} / p_{T_t}$.

Extracted values of $\langle j_T^2 \rangle$ as a function of p_{T_a} according to Eq. (16) are shown in Fig. 14. All $\langle j_T^2 \rangle$ values are constant in the explored region ($p_{T_a} > 1.5$ GeV/c).

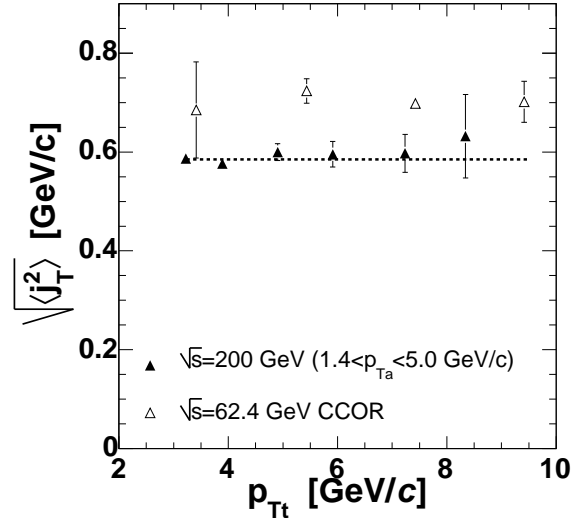


FIG. 15: Averaged values of $\langle j_T^2 \rangle$ in ($1.5 < p_{T_a} < 5$ GeV/c) as a function of the trigger transverse momentum p_{T_t} (solid triangles). The CCOR values measured at $\sqrt{s}=62.4$ GeV shown by open triangles.

It is expected that $\langle j_T^2 \rangle$ can not remain constant for arbitrarily small values of p_{T_a} because of the phase space limitation. In the region where $p_{T_a} \leq \sqrt{\langle j_T^2 \rangle}$, the magnitude of the j_T -vector is truncated, similar to the “Seagull effect” [44]. Since the $\sqrt{\langle j_T^2 \rangle}$ values are on the order of 600 MeV/c, we assume that the phase space limitation can be safely neglected for $p_{T_a} > 1.5$ GeV/c and we extract the values of $\sqrt{\langle j_T^2 \rangle}$ averaged over p_{T_a} and p_{T_t} (see Fig. 15)

$$\sqrt{\langle j_T^2 \rangle} = 585 \pm 6(\text{stat}) \pm 15(\text{sys}) \text{ MeV/c} \quad (24)$$

The systematic error originates from the finite momentum resolution and Eq. (16) where we assume that the arc-sine function can be approximated by its argument. For the angular width of the near angle peak (see Fig. 9 and Fig. 10) it corresponds to an uncertainty of order of 3%.

The independence of $\langle j_T^2 \rangle$ on either p_{T_t} or \sqrt{s} has been observed by the CCOR experiment in the range $\sqrt{s}=31\text{--}62.4$ GeV [1]. The $\langle j_T^2 \rangle$ values at $\sqrt{s}=62.4$ GeV (open triangles on Fig. 15) are systematically larger than values found in this analysis. The discrepancy should not be taken as significant, as CCOR used a slightly different technique than in this paper. CCOR extracted the $\langle j_T^2 \rangle$ values from measurements of $\langle |p_{\text{out}}| \rangle$ for different values of the x_E variable Eq. (19). According to Eq. (18) the $\langle |p_{\text{out}}| \rangle^2$ magnitude should depend linearly on x_E^2 ; and the $\langle |j_{T_y}| \rangle$ value was extracted from the intercept of the $\langle p_{\text{out}} \rangle^2(x_E)$ fit at $x_E=0$, rather than from a measurement of σ_N .

Knowing the $\langle j_T^2 \rangle$ and p_{out} values, we used Eq. (22) to determine $\hat{x}_h^{-1}(z_t) \sqrt{\langle k_T^2 \rangle}$ (see Fig. 16 and Fig. 17). The

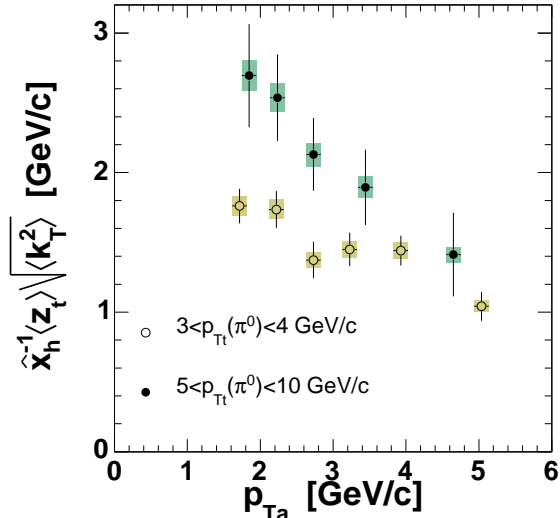


FIG. 16: (color online) $\hat{x}_h^{-1}\langle z_t \rangle \sqrt{\langle k_T^2 \rangle}$ values calculated according to Eq. (22) for trigger π^0 in $3 < p_{Tt} < 4$ GeV/c and $5 < p_{Tt} < 6$ GeV/c as a function of p_{Ta} . The systematic uncertainties are indicated by the shaded boxes.

systematic error was estimated with Monte Carlo simulations to be on the order of 5%. The main source of systematic error originates from the assumption (Eqs. (16) and (21)) of the relative smallness of $\langle j_T^2 \rangle$, collinearity between p_{out} and j_{Tay} and from the limited momentum resolution discussed in section III.

The p_{Ta} dependence of the extracted $\hat{x}_h^{-1}\langle z_t \rangle \sqrt{\langle k_T^2 \rangle}$ (Fig. 16) reveals a strikingly decreasing trend. It was originally expected that by fixing the value of p_{Tt} , the kinematics of the hard scattering (i.e. $\hat{p}_{Tt} \simeq \hat{p}_{Ta}$) would be fixed, independently of the value of p_{Ta} . Various values of p_{Ta} would then sample the \hat{p}_{Ta} fragmentation function, and the value of $\hat{x}_h^{-1}\langle z_t \rangle \sqrt{\langle k_T^2 \rangle}$ was expected to be constant. It is evident that this assumption is not quite correct.

A similar line of argument applies also for the rising trend when p_{Ta} is fixed and p_{Tt} varies (Fig. 17). It is interesting to note that the CCOR $\sqrt{\langle k_T^2 \rangle}$ values measured at $\sqrt{s}=62.4$ GeV (open triangles on Fig. 17) reveal a similar rising trend. However, the rising trend of $\hat{x}_h^{-1}\langle z_t \rangle \sqrt{\langle k_T^2 \rangle}$ with p_{Tt} and falling with p_{Ta} suggests that the variation of $\sqrt{\langle k_T^2 \rangle}$ with p_{Tt} seen by the CCOR collaboration [1] may be indicative of the $\langle z_t \rangle \hat{x}_h^{-1}$ variation which was there neglected.² In order to understand variation of $\langle z_t \rangle$ and \hat{x}_h we have to explore the process

² Note, however that the method was different. CCOR determined j_T and k_T from the slope and intercept of Eq. 21 with respect to p_{Ta} at each value of p_{Tt} , with the implicit assumption that $\langle z_t \rangle \hat{x}_h^{-1} = 1$.

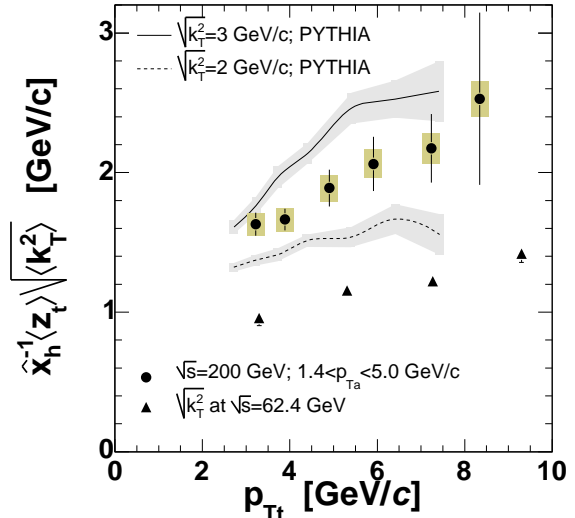


FIG. 17: (color online) The same calculation according Eq. (22) for fixed associated bin $1.4 < p_{Ta} < 5.0$ GeV/c as a function of p_{Tt} . The systematic errors indicated by colored rectangles. The $\sqrt{\langle k_T^2 \rangle}$ results obtained by CCOR collaboration at $\sqrt{s}=62.4$ GeV [1] displayed by solid triangles.

of dijet fragmentation.

V. FRAGMENTATION FUNCTIONS

We have shown in Eq. (22) that the width of the away side correlation peak

is related to the product of $\hat{x}_h^{-1}\langle z_t \rangle \sqrt{\langle k_T^2 \rangle}$. In order to evaluate $\langle z_t \rangle$, knowledge of the scattered parton \hat{p}_T spectrum and fragmentation function is required.

Fragmentation functions from e^+e^- collisions, weighted by the appropriate hard-scattering constituent cross-sections and Q^2 evolution could in principle be used. However, it was originally thought that the shape of the fragmentation function could be deduced from present measurements using the combined analysis of the inclusive trigger p_{Tt} and associated particle p_{Ta} distributions. Although this idea turned out to be incorrect, we will follow this line of reasoning for a while as it is instructive.

Generally, the invariant cross section for inclusive hadron production from jets can be parametrized in the following way. First, we assume that the number of parton fragments (consider only pions for simplicity) at a given p_T corresponds to the sum over all contributions from parton momenta, \hat{p}_T from $p_T < \hat{p}_T < \sqrt{s}/2$. The joint probability of detecting a pion with $p_T = z\hat{p}_T$ originating from a parton with \hat{p}_T can be written as

$$\frac{d^2\sigma_\pi}{\hat{p}_T d\hat{p}_T dz} = \frac{d\sigma_q}{\hat{p}_T d\hat{p}_T} \times D_\pi^q(z)$$

$$= f_q(\hat{p}_T) \times D_\pi^q(z). \quad (25)$$

Here we use $f_q(\hat{p}_T)$ to represent the final state scattered-parton invariant spectrum $d\sigma_q/\hat{p}_T d\hat{p}_T$ and $D_\pi^q(z)$ to represent the fragmentation function. The first term in Eq. (25) can be viewed as a probability of finding a parton with transverse momentum \hat{p}_T and the second term corresponds to the probability that the parton fragments into a particle of momentum $p_T = z\hat{p}_T$. With a simple change of variables from \hat{p}_T to $p_T = z\hat{p}_T$, we obtain the joint probability of a pion with p_T which is a fragment with momentum fraction z from a parton with $\hat{p}_T = p_T/z$:

$$\frac{d^2\sigma_\pi}{p_T dp_T dz} = f_q\left(\frac{p_T}{z}\right) \cdot D_\pi^q(z) \frac{1}{z^2}. \quad (26)$$

The p_T and z dependences do not factorize. However, the p_T spectrum may be found by integrating over all values of $\hat{p}_T \geq p_T$ to $\hat{p}_{Tmax} = \sqrt{s}/2$, which corresponds to values of z from $x_T = 2p_T/\sqrt{s}$ to 1.

$$\frac{1}{p_T} \frac{d\sigma_\pi}{dp_T} = \int_{x_T}^1 f_q\left(\frac{p_T}{z}\right) \cdot D_\pi^q(z) \frac{dz}{z^2} \quad (27)$$

Alternatively, for any fixed value of p_T one can evaluate the $\langle z(p_T) \rangle$, integrated over the parton spectrum:

$$\langle z(p_T) \rangle = \frac{\int_{x_T}^1 z D_\pi^q(z) f_q(\hat{p}_T) (p_T/z) \frac{dz}{z^2}}{\int_{x_T}^1 D_\pi^q(z) f_q(p_T/z) \frac{dz}{z^2}}. \quad (28)$$

From the scaling properties of QCD and from the shape of the π^0 invariant cross section itself, which is a pure power law for $p_T \geq 3$ GeV/c [37], one can deduce that $f_q(\hat{p}_T)$ should have a power law shape, $f_q(\hat{p}_T) = A\hat{p}_T^{-n}$. In this case the hadron spectrum also has a power law shape because

$$\begin{aligned} \frac{1}{p_T} \frac{d\sigma_\pi}{dp_T} &\approx \int_{x_T}^1 A D_\pi^q(z) \cdot \left(\frac{p_T}{z}\right)^{-n} \frac{dz}{z^2} \\ &\approx \frac{A}{p_T^n} \int_{x_T}^1 D_\pi^q(z) \cdot z^{n-2} dz \end{aligned} \quad (29)$$

and the last integral depends only weakly on p_T due to the small value of x_T . For small parton \hat{p}_T (below 3-4 GeV/c) the power law shape is no longer valid, but the region $p_T < 3$ GeV/c is outside the scope of this paper. The $f_q(\hat{p}_T)$ should also diminish for very high $\hat{p}_T \rightarrow \sqrt{s}/2$ where the phase space available for hard parton production diminishes, again not relevant for the present purposes.

We used the power law parameterization for the final state scattered-parton invariant spectrum $f_q(\hat{p}_T) \propto \hat{p}_T^{-n}$ where n is a free parameter which can be determined from the fit of Eq. (27) to the measured π^0 cross section. There is, however, one more missing piece of information - the shape of the fragmentation function D_π^q . In an attempt to extract this information from the data, we have analyzed associated x_E -distributions, as shown in Table VII.

A. 'Scaling' variable x_E

It was expected [2] that the x_E variable, defined by Eq. (19), to first order, approximates the fragmentation function in the limit of high values of p_{Tt} , where there is sufficient collinearity between the trigger particle and the fragmenting parton. In this case where $j_T \ll p_{Tt}$ and $k_T \ll p_{Tt}$ one can assume that $p_{Tt} = \hat{p}_{Tt}/z_t$ and $x_E z_t = \hat{x}_h p_{Tt} \cos \Delta\phi / \hat{p}_{Tt} \simeq \hat{x}_h z_a$, and thus the slopes of $D(z_a)$ and x_E are related as

$$\langle z_a \rangle \approx \langle x_E \rangle \langle z_t \rangle \hat{x}_h^{-1}. \quad (30)$$

The x_E distributions of particles associated with trigger particles in the 3-8 GeV/c range of transverse momentum are plotted in Fig. 18. The dashed lines represent exponential fits. The slopes of these exponentials range from -5.8 ($3 < p_{Tt} < 4$ GeV/c) to -7.8 (open symbols on Fig. 19). This is qualitatively and quantitatively different from the similar measurement done by CCOR collaboration at $\sqrt{s}=62.4$ GeV where the slopes of exponential fits to the x_E distributions were found to be ≈ -5.3 and independent of the trigger transverse momenta. That observation also supported the hypothesis of the x_E distribution being a good approximation of the fragmentation function. We also note that the x_E distributions are not quite exponential and at large values of x_E there is a tail similar to the power law tail of the single inclusive p_T distribution.

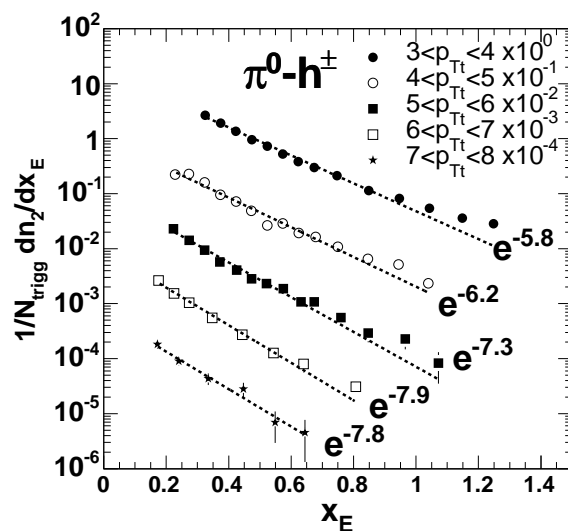


FIG. 18: The distribution of associated particles with x_E variable for various trigger particle p_{Tt} indicated in the legend. Exponential fits indicated by dashed lines.

The reason why the x_E distributions do not have the same slope for different p_{Tt} and why there is a “power law” tail at large x_E is the same as that which causes $\hat{x}_h^{-1} \langle z_t \rangle \sqrt{\langle k_T^2 \rangle}$ to decrease with the associated particle transverse momentum. It turns out that by sampling

TABLE VII: Measured x_E distributions associated with various transverse momenta of the trigger π^0 . Only the statistical errors are shown.

	$p_{Tt}=3.39$ GeV/c		$p_{Tt}=4.40$ GeV/c		$p_{Tt}=5.41$ GeV/c		$p_{Tt}=6.40$ GeV/c		$p_{Tt}=7.39$ GeV/c		
x_E	dn/dx_E	x_E	dn/dx_E	x_E	dn/dx_E	x_E	dn/dx_E	x_E	dn/dx_E	x_E	dn/dx_E
0.32	$2.7e+00 \pm 4.7e-02$	0.23	$6.7e-01 \pm 2.2e-02$	0.22	$2.3e-01 \pm 1.2e-02$	0.18	$8.0e-02 \pm 6.3e-03$	0.17	$1.8e-02 \pm 3.1e-03$		
0.37	$1.9e+00 \pm 4.0e-02$	0.27	$6.8e-01 \pm 2.2e-02$	0.27	$1.4e-01 \pm 9.6e-03$	0.22	$4.6e-02 \pm 4.7e-03$	0.24	$9.0e-03 \pm 1.5e-03$		
0.42	$1.4e+00 \pm 3.3e-02$	0.32	$4.8e-01 \pm 1.9e-02$	0.32	$9.4e-02 \pm 7.7e-03$	0.27	$3.1e-02 \pm 3.9e-03$	0.33	$4.4e-03 \pm 1.0e-03$		
0.47	$9.6e-01 \pm 2.8e-02$	0.37	$2.9e-01 \pm 1.4e-02$	0.37	$5.7e-02 \pm 6.0e-03$	0.35	$1.7e-02 \pm 2.0e-03$	0.45	$2.8e-03 \pm 8.1e-04$		
0.52	$7.3e-01 \pm 2.4e-02$	0.42	$2.2e-01 \pm 1.2e-02$	0.43	$4.1e-02 \pm 5.0e-03$	0.44	$8.2e-03 \pm 1.4e-03$	0.55	$6.9e-04 \pm 4.0e-04$		
0.57	$5.2e-01 \pm 2.0e-02$	0.47	$1.5e-01 \pm 1.0e-02$	0.47	$2.8e-02 \pm 4.2e-03$	0.54	$3.8e-03 \pm 9.2e-04$	0.64	$4.5e-04 \pm 3.2e-04$		
0.62	$3.8e-01 \pm 1.7e-02$	0.52	$8.0e-02 \pm 7.4e-03$	0.52	$2.3e-02 \pm 3.8e-03$	0.64	$2.4e-03 \pm 7.3e-04$				
0.67	$3.0e-01 \pm 1.5e-02$	0.57	$8.6e-02 \pm 7.7e-03$	0.57	$1.9e-02 \pm 3.4e-03$	0.81	$9.3e-04 \pm 2.6e-04$				
0.75	$2.1e-01 \pm 9.0e-03$	0.62	$5.8e-02 \pm 6.3e-03$	0.63	$1.1e-02 \pm 2.5e-03$						
0.85	$1.1e-01 \pm 6.5e-03$	0.68	$4.9e-02 \pm 5.7e-03$	0.67	$1.1e-02 \pm 2.5e-03$						
0.95	$8.2e-02 \pm 5.5e-03$	0.75	$3.2e-02 \pm 3.3e-03$	0.76	$5.6e-03 \pm 1.3e-03$						
1.04	$5.4e-02 \pm 4.5e-03$	0.85	$2.0e-02 \pm 2.5e-03$	0.85	$2.9e-03 \pm 9.2e-04$						
1.15	$3.6e-02 \pm 3.6e-03$	0.94	$1.6e-02 \pm 2.2e-03$	0.97	$2.3e-03 \pm 8.1e-04$						
1.25	$2.8e-02 \pm 3.2e-03$	1.04	$7.0e-03 \pm 1.5e-03$	1.07	$8.3e-04 \pm 4.8e-04$						

different regions of p_{Ta} for fixed p_{Tt} , the average momentum of the parton fragmenting into a trigger particle, $\langle z_t \rangle$, also changes. This kind of trigger bias causes the hard scattering kinematics, the value of \hat{p}_T , to not be fixed for the case where p_{Tt} is fixed but p_{Ta} varies.

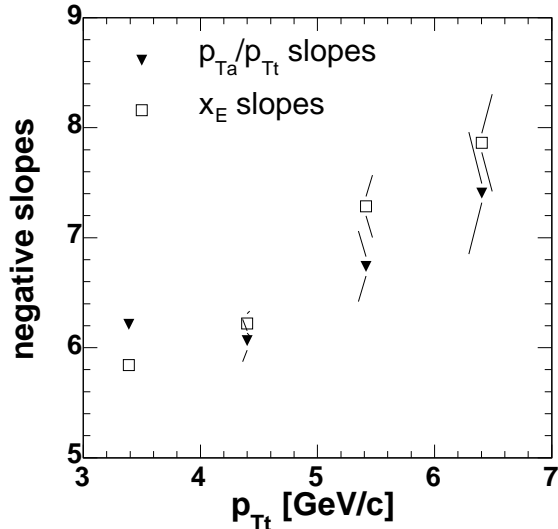


FIG. 19: The negative slope parameters extracted from the fit of a plain exponential function into a x_E (see Fig. 18) and p_{Ta}/p_{Tt} (see Fig. 20) distributions.

Taking this into account, one can not treat the associated x_E distribution as a rescaled fragmentation function, but rather as a folding of the two fragmentation processes of trigger and associated jets. The same line of arguments applies also for other two-particle variables, *e.g.* p_{Ta}/p_{Tt} , [45] used for an approximation of the fragmentation variable z (see Fig. 20). The negative slopes of an exponential fit in the $0.2 < p_{Ta}/p_{Tt} < 0.4$ range (solid symbols on Fig. 19) are, within the error bars,

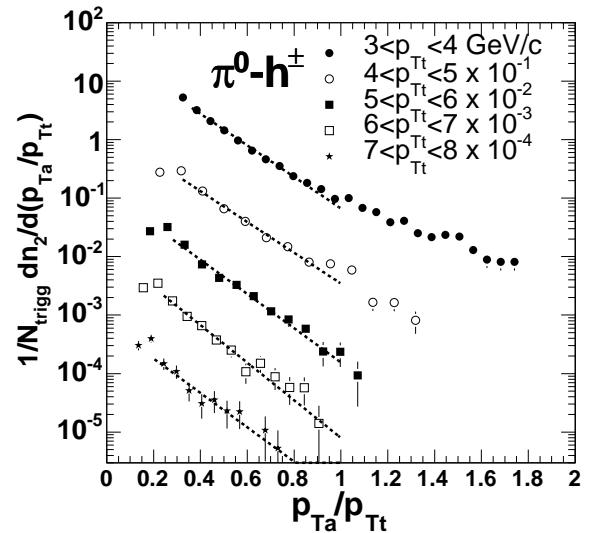


FIG. 20: The distribution of associated particles with p_{Ta}/p_{Tt} variable for various trigger particle p_{Tt} indicated in the legend. The distribution were fitted in the limited range $0.2 < p_{Ta}/p_{Tt} < 0.4$ by an exponential function (dashed lines).

the same as for x_E .

In conclusion: the slope parameters extracted from associated x_E distributions reveal the rising trend with p_{Tt} which reflects the fact, that the different p_{Ta} samples not only different z_a but also different z_t .

The description of an associated distribution detected under the condition of the existence of a trigger particle requires an extension of the formulae discussed in V and is a subject of the next section.

VI. DIJET FRAGMENTATION

For the description of the detection of a single particle which is the result of jet fragmentation, recall Eq. (25)

$$\begin{aligned} \frac{d^2\sigma_\pi}{d\hat{p}_T dz_t} &= \frac{d\sigma_q}{d\hat{p}_T} \times D_\pi^q(z_t) \\ &= \hat{p}_T f_q(\hat{p}_T) \times D_\pi^q(z_t) \equiv \Sigma_q(\hat{p}_T) \times D_\pi^q(z_t) \end{aligned} \quad (31)$$

where we have now explicitly labeled the z of the trigger particle as z_t , and defined

$$\Sigma_q(\hat{p}_T) \equiv \hat{p}_T f_q(\hat{p}_T) = \frac{d\sigma_q}{d\hat{p}_T} \quad . \quad (32)$$

When k_T smearing is introduced, configurations for which the high p_T parton pair is on the average moving towards the trigger particle are favored due to the steeply falling \hat{p}_T spectrum, such that:

$$\langle \hat{p}_{Tt} - \hat{p}_T \rangle \simeq \frac{1}{2} \langle \hat{p}_{Tt} - \hat{p}_{Ta} \rangle \equiv s(k_T)$$

with small variance σ_s^2 , and we explicitly introduced \hat{p}_{Tt} and \hat{p}_{Ta} to represent the transverse momenta of the trigger and away partons. The single inclusive p_{Tt} spectrum is now given by

$$\frac{d^2\sigma_\pi}{d\hat{p}_{Tt} dz_t} = \Sigma'_q(\hat{p}_{Tt}) \times D_\pi^q(z_t) \quad (33)$$

where the trigger parton \hat{p}_{Tt} spectrum after k_T smearing is

$$\Sigma'_q(\hat{p}_{Tt}) \equiv \hat{p}_{Tt} f'_q(\hat{p}_{Tt}) = \frac{d\sigma_q}{d\hat{p}_{Tt}} \quad . \quad (34)$$

Then, the conditional probability for finding the away side parton with \hat{p}_{Ta} and z_a , given \hat{p}_{Tt} (and z_t), is:

$$\left. \frac{dP(\hat{p}_{Ta}, z_a)}{d\hat{p}_{Ta} dz_a} \right|_{\hat{p}_{Tt}} = C(\hat{p}_{Ta}, \hat{p}_{Tt}, k_T) D_\pi^q(z_a)$$

where $C(\hat{p}_{Ta}, \hat{p}_{Tt}, k_T)$ represents the distribution of the transverse momentum of the away parton \hat{p}_{Ta} , given \hat{p}_{Tt} and k_T , which can be written as:

$$\begin{aligned} C(\hat{p}_{Ta}, \hat{p}_{Tt}, k_T) &= \\ &= \frac{1}{\sqrt{2\pi\sigma_s^2}} \exp\left(\frac{-[\hat{p}_{Ta} - (\hat{p}_{Tt} - 2s(k_T))]}{2\sigma_s^2}\right)^2. \end{aligned} \quad (35)$$

Then

$$\frac{d^4\sigma_\pi}{d\hat{p}_{Tt} dz_t d\hat{p}_{Ta} dz_a} = \frac{d^2\sigma_\pi}{d\hat{p}_{Tt} dz_t} \times \left. \frac{dP(\hat{p}_{Ta}, z_a)}{d\hat{p}_{Ta} dz_a} \right|_{\hat{p}_{Tt}} \quad .$$

In general, $\sigma_s/s(k_T)$ is small (see section VIB) so that $C(\hat{p}_{Ta}, \hat{p}_{Tt}, k_T)$ is well approximated by a δ function and we may take

$$\hat{p}_{Ta} = \hat{p}_{Tt} - 2s(k_T) = \hat{x}_h \hat{p}_{Tt} \quad ,$$

so that

$$\frac{d^3\sigma_\pi}{d\hat{p}_{Tt} dz_t dz_a} = \Sigma'_q(\hat{p}_{Tt}) D_\pi^q(z_t) D_\pi^q(z_a)$$

where

$$z_a = \frac{p_{Ta}}{\hat{p}_{Ta}} = \frac{p_{Ta}}{\hat{x}_h \hat{p}_{Tt}} = \frac{z_t p_{Ta}}{\hat{x}_h p_{Tt}} \quad .$$

Changing variables from \hat{p}_{Tt} , z_t to p_{Tt} , z_t as above, and similarly from z_a to p_{Ta} , we obtain

$$\frac{d^3\sigma_\pi}{dp_{Tt} dz_t dp_{Ta}} = \frac{1}{\hat{x}_h p_{Tt}} \Sigma'_q\left(\frac{p_{Tt}}{z_t}\right) D_\pi^q(z_t) D_\pi^q\left(\frac{z_t p_{Ta}}{\hat{x}_h p_{Tt}}\right) \quad (36)$$

where for integrating over z_t or finding $\langle z_t \rangle$ for fixed p_{Tt} , p_{Ta} , the minimum value of z_t is $z_t^{\min} = 2p_{Tt}/\sqrt{s} = x_{Tt}$ and the maximum value is:

$$z_t^{\max} = \hat{x}_h \frac{p_{Tt}}{p_{Ta}} = \frac{\hat{x}_h}{x_h} \quad ,$$

where $\hat{x}_h(p_{Tt}, p_{Ta})$ is also a function of k_T (Eq. (20)).

Thus, in order to evaluate $\hat{x}_h(p_{Tt}, p_{Ta})$ for use in Eq. (36), k_T must be known. We attack this problem by successive approximations. First we solve for k_T and $D_\pi^q(z)$ assuming $\hat{x}_h = 1$ as done at the ISR where the smearing correction was small. Then we solve for $\hat{x}_h(p_{Tt}, p_{Ta})$ with this value of k_T and iterate. On the first solution we solve only for $\Sigma'_q(\hat{p}_{Tt})$ while on the iteration we include the k_T smearing to solve for the unsmear parton spectrum $\Sigma_q(\hat{p}_T) = \hat{p}_T f_q(\hat{p}_T)$ (Eq. (32)).

A. Sensitivity of the associated spectra to the fragmentation function

As discussed in section V A, the associated x_E distribution was thought to approximate the fragmentation function of the away jet. Equation 36 can be transformed to the x_E distribution at fixed p_{Tt} with a change of variables from p_{Ta} to x_E followed by integration over z_t :

$$\begin{aligned} \frac{d^2\sigma}{dp_{Tt} dx_E} &= \frac{dp_{Ta}}{dx_E} \times \frac{d^2\sigma}{dp_{Tt} dp_{Ta}} \simeq \\ &= \frac{1}{\hat{x}_h} \int_{x_{Tt}}^{\hat{x}_h \frac{p_{Tt}}{p_{Ta}}} D_\pi^q(z_t) D_\pi^q\left(\frac{z_t p_{Ta}}{\hat{x}_h p_{Tt}}\right) \Sigma'_q\left(\frac{p_{Tt}}{z_t}\right) dz_t. \end{aligned} \quad (37)$$

We at first attempted to solve for the fragmentation function by simultaneous fits of the measured x_E distributions to Eq. (37) constrained by a fit of the inclusive invariant π^0 cross section to Eq. (27). There were difficulties with convergence.

The reason for the lack of convergence became apparent when we calculated x_E distributions according to

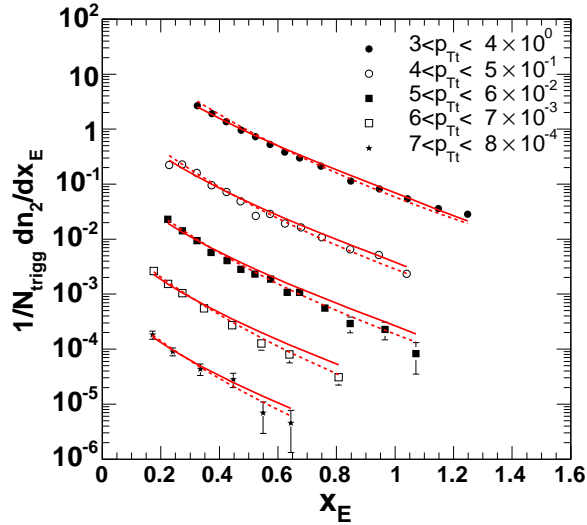


FIG. 21: (color online) The same x_E distributions as on Fig. 18 shown with calculations according to Eq. (37) for quark (solid lines) and for gluon (dashed lines) $D(z)$. An exponential approximation was used and the slopes for quark and gluon fragmentation function were obtained by fitting to LEP data [46] and [47] (see Fig. 22).

Eq. (37) (Fig. 21) for two different fragmentation functions corresponding to quark and gluon jet fragmentation. A simple exponential parameterization was used and the slopes were obtained from the fit to the LEP data [46], [47] (Fig. 22). For quark and gluon jets, we found $D_q(z) \approx \exp(-8.2 \cdot z)$ and $D_g(z) \approx \exp(-11.4 \cdot z)$ respectively. For the parton final state spectrum, we used $\Sigma'_q \propto \hat{p}_T^{-8}$. It is evident that the x_E distributions calculated for the quite different quark and gluon fragmentation functions do not differ significantly (the difference between solid and dashed lines on Fig. 21). Clearly, the x_E distributions are rather insensitive to the fragmentation functions of the away jet in contradiction to the previous conventional wisdom. The evidence of this explicit counter example led to attempts to perform the integrals of Eq. (36) and Eq. (33) analytically which straightforwardly confirmed the observation that the x_E distribution is not sensitive to the fragmentation function.

If the smeared trigger parton spectrum is taken as a power law,

$$\Sigma'_q\left(\frac{p_{Tt}}{z_t}\right) = A\left(\frac{p_{Tt}}{z_t}\right)^{-(n-1)}$$

and the fragmentation function as an exponential, $D(z) = B \exp(-bz)$, then the integral of Eq. (36) over z_t becomes:

$$\frac{d\sigma_\pi}{dp_{Tt} dp_{Ta}} = \quad (38)$$

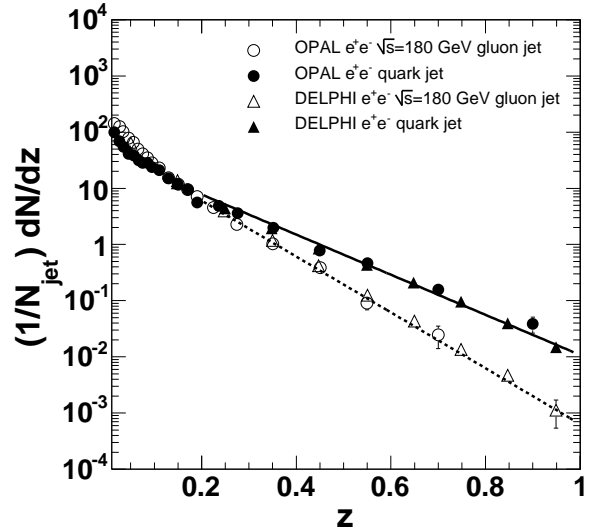


FIG. 22: Fragmentation function measured in e^+e^- collisions at $\sqrt{s}=180$ GeV for gluon and quark jets. The solid and dashed lines represent the exponential fit in the $0.2 < z < 1$ region.

$$\frac{B^2}{\hat{x}_h} \frac{A}{p_{Tt}^n} \int_{x_{Tt}}^{\hat{x}_h \frac{p_{Tt}}{p_{Ta}}} dz_t z_t^{n-1} \exp[-bz_t(1 + \frac{p_{Ta}}{\hat{x}_h p_{Tt}})]$$

which is an incomplete gamma function. Since $\hat{x}_h \sim 1$, we make the assumption that it is constant. Similarly, the integrals of Eqs. 29, 33 are also incomplete gamma functions:

$$\frac{d\sigma_\pi}{dp_{Tt}} = \frac{AB}{p_{Tt}^{n-1}} \int_{x_{Tt}}^1 dz_t z_t^{n-2} \exp[-bz_t] \quad (39)$$

A reasonable approximation for the inclusive single, and two particle cross sections is obtained by taking the lower limit to zero and the upper limit to infinity, leading to the replacement of the incomplete gamma functions by gamma functions, with the result that:

$$\frac{d^2\sigma_\pi}{dp_{Tt} dp_{Ta}} \approx \frac{\Gamma(n) B^2 A}{b^n} \frac{1}{\hat{x}_h p_{Tt}^n (1 + \frac{p_{Ta}}{\hat{x}_h p_{Tt}})^n} \quad (40)$$

$$\frac{d\sigma_\pi}{dp_{Tt}} \approx \frac{\Gamma(n-1) AB}{b^{n-1} p_{Tt}^{n-1}}, \quad (41)$$

where $\Gamma(n) = (n-1)\Gamma(n-1)$.

The conditional probability is just the ratio of the joint probability Eq. (40) to the inclusive probability Eq. (41), or

$$\left. \frac{dP_\pi}{dp_{Ta}} \right|_{p_{Tt}} \approx \frac{B(n-1)}{b p_{Tt}} \frac{1}{\hat{x}_h} \frac{1}{(1 + \frac{p_{Ta}}{\hat{x}_h p_{Tt}})^n} \quad (42)$$

In the collinear limit, where $p_{Ta} = x_E p_{Tt}$:

$$\left. \frac{dP_\pi}{dx_E} \right|_{p_{Tt}} \approx \frac{B(n-1)}{b} \frac{1}{\hat{x}_h} \frac{1}{(1 + \frac{x_E}{\hat{x}_h})^n} \quad (43)$$

The only dependence on the fragmentation function, in this approximation, is in the normalization constant B/b which equals $\langle m \rangle$, the multiplicity in the away-jet from the integral of the fragmentation function. The dominant term in Eq. (43) is the Hagedorn function $1/(1+x_E/\hat{x}_h)^n$, so that at fixed p_{Tt} the x_E distribution is predominantly a function only of x_E and thus does exhibit ‘ x_E ’ scaling. Also, the Hagedorn function explains the ‘power law’ tail at large x_E noted in section V A. The reason that the x_E distribution is not very sensitive to the fragmentation function is that the integral over z_t for fixed p_{Tt} and p_{Ta} (Eq. (38)) is actually an integral over the jet transverse momentum \hat{p}_{Tt} . However since both the trigger and away jets are always roughly equal and opposite in transverse momentum, integrating over \hat{p}_{Tt} simultaneously integrates over \hat{p}_{Ta} , and thus also integrates over the away jet fragmentation function. This can be seen directly by the presence of z_t in both the same and away fragmentation functions in Eqs. 36 and 37, so that the integral over z_t integrates over both fragmentation functions simultaneously.

B. k_T smearing

In order to evaluate $\hat{x}_h(p_{Tt}, p_{Ta})$ and k_T must be known. We attack this problem by successive approximations: first we solve for k_T assuming $\hat{x}_h = 1$ as done at the ISR, where the smearing correction was small. Then we iterate for finite k_T . The Gaussian approximation for the smearing function Eq. (35) does not work so well in the low \hat{p}_T region. The product of the steeply

falling parton distribution function and the fragmentation function is peaked at $z \approx 1$ preferring ‘small’ parton momenta. We have developed more accurate description of the conditional yields taking into account the k_T smearing.

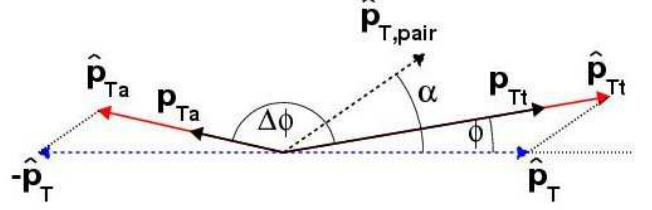


FIG. 23: (color online) Back-to-back partons in hard scattering rest frame (blue dashed arrows) with four-momenta $(\hat{p}_T, 0, 0, \hat{p}_T)$ and $(-\hat{p}_T, 0, 0, \hat{p}_T)$ in $(-, -, +)$ metrics moving along \hat{p}_n ($\hat{p}_n = \hat{p}_{T\text{pair}}$) for an event where detection of p_{Tt} and p_{Ta} is required (the j_T contribution is neglected). The $p_{Tt} > p_{Ta}$ condition implies that the events with \hat{p}_n pointing more in the direction of p_{Tt} are selected.

Let us consider the configuration depicted on Fig. 23. The two back-to-back partons in \hat{s} frame undergo the Lorentz boost determined by net pair momentum

$$\vec{p}_n \equiv \vec{p}_{T\text{pair}} \equiv \vec{p}_{Tt} + \vec{p}_{Ta} = \vec{k}_{Tt} + \vec{k}_{Ta} \quad (44)$$

If we denote an angle between the unsmeared parton momentum and k_T -vector (or \vec{p}_n) as α (see Fig. 23) then we can write the conditional probability distribution of trigger parton momenta, \hat{p}_{Tt} , as

$$\frac{d^3\sigma}{d\hat{p}_{Tt} d\alpha d\hat{p}_T} \Big|_{p_{Tt}, p_{Ta}} = \hat{p}_{Tt} \cdot \Sigma_q(\hat{p}_T) \cdot \hat{p}_n \cdot G(\hat{p}_n(\vec{r}_t)) \cdot D_\pi^q\left(\frac{p_{Tt}}{\hat{p}_{Tt}}\right) \frac{p_{Tt}}{\hat{p}_{Tt}^2} \cdot D_\pi^q\left(\frac{p_{Ta}}{\hat{p}_{Ta}(\vec{r}_t)}\right) \frac{p_{Ta}}{\hat{p}_{Ta}^2(\vec{r}_t)} \quad (45)$$

where $G(\hat{p}_n) = \exp(-\hat{p}_n^2/2\langle k_T^2 \rangle)$ describes the Gaussian probability distribution of the net pair momentum magnitude distribution, $\Sigma_q(\hat{p}_T)$ is the unsmeared parton momentum distribution, D_π^q is the fragmentation function and $\vec{r}_t = (\hat{p}_{Tt}, \phi, \hat{p}_T, k_T)$ is the phase space vector. The \hat{p}_{Tt} is chosen to be an integration variable and \hat{p}_{Ta} is fully determined by given values of \hat{p}_{Tt} , \hat{p}_T , angle ϕ and by the requirement of Lorentz invariance.

In order to evaluate $\langle z_t(k_T) \rangle \Big|_{p_{Tt}, p_{Ta}}$ and $\hat{x}_h(k_T) \Big|_{p_{Tt}, p_{Ta}}$ we have to evaluate first the parton distribution for events where given p_{Tt} and p_{Ta} are detected. This conditional cross section can be expressed as a definite integral over the unobserved variables ϕ and \hat{p}_T (see Fig. 23)

$$\frac{d\sigma}{d\hat{p}_{Tt}} \Big|_{p_{Tt}, p_{Ta}} = 2 \int_0^{\sqrt{s}/2} \int_0^\pi \frac{d^3\sigma}{d\hat{p}_{Tt} d\hat{p}_T d\phi} \Big|_{p_{Tt}, p_{Ta}} d\phi d\hat{p}_T$$

$$= D_\pi^q\left(\frac{p_{Tt}}{\hat{p}_{Tt}}\right) \frac{2}{\hat{p}_{Tt}} \int_0^{\sqrt{s}/2} \Sigma_q(\hat{p}_T) \times \int_0^\pi \hat{p}_n(\vec{r}_t) G(\hat{p}_n(\vec{r}_t)) \cdot D_\pi^q\left(\frac{p_{Ta}}{\hat{p}_{Ta}(\vec{r}_t)}\right) \frac{1}{\hat{p}_{Ta}^2(\vec{r}_t)} d\phi d\hat{p}_T \quad (46)$$

The $d\sigma/d\hat{p}_{Ta} \Big|_{p_{Tt}, p_{Ta}}$ distribution can be derived from Eq. (46) just by rotation $\hat{p}_{Tt} \rightarrow \hat{p}_{Ta}$ and $\hat{p}_{Ta} \rightarrow \hat{p}_{Tt}$. The $\langle z_t(k_T) \rangle \Big|_{p_{Tt}, p_{Ta}}$ and $\hat{x}_h(k_T) \Big|_{p_{Tt}, p_{Ta}}$ quantities can then be evaluated as

$$\langle z_t(k_T) \rangle \Big|_{p_{Tt}, p_{Ta}} = \frac{Z(1)}{Z(0)} \quad (47)$$

where

$$Z(n) = \int_{x_{Tt}}^1 z_t^{n-1} D_\pi^q(z_t) \int_0^{\sqrt{s}/2} \Sigma_q(\hat{p}_T) \times \int_0^\pi \hat{p}_n G(\hat{p}_n(\vec{r}_{zt})) \cdot D_\pi^q\left(\frac{p_{Ta}}{\hat{p}_{Ta}(\vec{r}_{zt})}\right) \frac{1}{\hat{p}_{Ta}^2(\vec{r}_{zt})} d\phi d\hat{p}_T dz_t$$

and $\vec{r}_{zt} = (p_{Tt}/z_t, \phi, \hat{p}_T, k_T)$. The $\hat{x}_h(k_T)|_{p_{Tt}, p_{Ta}}$ is evaluated as

$$\hat{x}_h(k_T)|_{p_{Tt}, p_{Ta}} = \frac{\langle \hat{p}_{Ta} \rangle}{\langle \hat{p}_{Tt} \rangle}|_{p_{Tt}, p_{Ta}} = \frac{\mathcal{X}_a(1) \mathcal{X}_t(0)}{\mathcal{X}_a(0) \mathcal{X}_t(1)} \quad (48)$$

where

$$\begin{aligned} \mathcal{X}_t(n) &= \int_{p_{Tt}}^{\sqrt{s}/2} \hat{p}_{Tt}^{n-1} D_\pi^q\left(\frac{p_{Tt}}{\hat{p}_{Tt}}\right) \int_0^{\sqrt{s}/2} \Sigma_q(\hat{p}_T) \times \\ &\times \int_0^\pi \hat{p}_n(\vec{r}_t) G(\hat{p}_n(\vec{r}_t)) \cdot D_\pi^q\left(\frac{p_{Ta}}{\hat{p}_{Ta}(\vec{r}_t)}\right) \frac{1}{\hat{p}_{Ta}^2(\vec{r}_t)} d\phi d\hat{p}_T \hat{p}_{Tt} \\ \mathcal{X}_a(n) &= \int_{p_{Ta}}^{\sqrt{s}/2} \hat{p}_{Ta}^{n-1} D_\pi^q\left(\frac{p_{Ta}}{\hat{p}_{Ta}}\right) \int_0^{\sqrt{s}/2} \Sigma_q(\hat{p}_T) \times \\ &\times \int_0^\pi \hat{p}_n(\vec{r}_a) G(\hat{p}_n(\vec{r}_a)) \cdot D_\pi^q\left(\frac{p_{Tt}}{\hat{p}_{Tt}(\vec{r}_a)}\right) \frac{1}{\hat{p}_{Tt}^2(\vec{r}_a)} d\phi d\hat{p}_T \hat{p}_{Ta} \end{aligned}$$

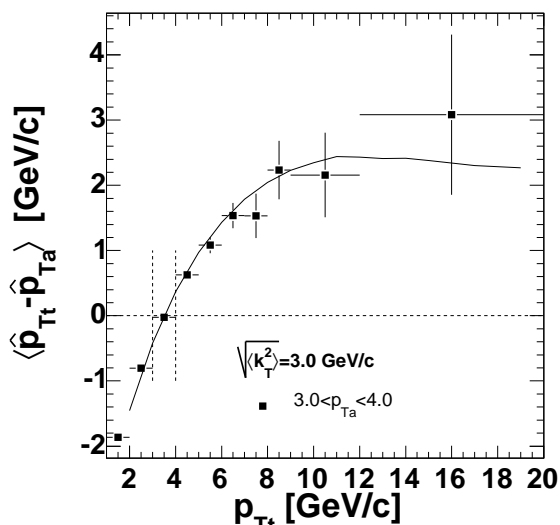


FIG. 24: PYTHIA simulated average momentum unbalance for the associated particles in $3.0 < p_{Ta} < 4.0$ GeV/c bin and calculated according Eq. (48). The two vertical dashed line indicates the range where p_{Tt} and p_{Ta} are equal and the parton momenta unbalance vanishes (fixed correlations).

We have tested the above formulae on PYTHIA simulation. We have generated events with $\sqrt{\langle k_T^2 \rangle} = 3$ GeV/c and evaluated the partons' momenta unbalance variation with p_{Tt} for fixed $3 < p_{Ta} < 4$ GeV/c bin. The results from the PYTHIA simulation (solid point on Fig. 24) are compared to calculation based on Eq. (48) (solid line on Fig. 24). The magnitude of momentum unbalance saturates at $p_{Tt} \approx 10$ GeV/c around $\sqrt{\langle k_{Tx}^2 \rangle}$ and then starts to decrease. The maximum value depends on the the k_T magnitude and on the asymmetry between p_{Tt} and p_{Ta} . Eventually, the unbalance should vanish at high p_{Tt} as a consequence of $\Sigma_q(\hat{p}_T)$ flattening.

The comparison of $\langle z_t \rangle$ and $\langle z_a \rangle$ found in PYTHIA and derived according to Eq. (47) is shown in Fig. 25.

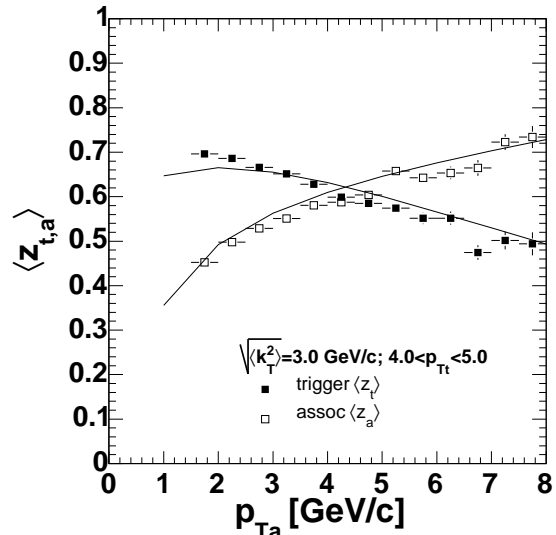


FIG. 25: Average z of a trigger and associated particle as a function of p_{Ta} from PYTHIA and according Eq. (47).

The overall agreement between the PYTHIA simulations and the calculation is excellent. The small deviations may be attributed to the fact that in the PYTHIA simulation, 1 GeV/c-wide bins were used for trigger and associated particle identification, whereas the calculation was performed for fixed values of p_{Tt} and p_{Ta} .

The last missing piece of information needed before solving Eq. (22) is the fragmentation function D_π^q and unsmeared $\Sigma_q(\hat{p}_T)$. The description of how this knowledge was extracted from the data is a subject of next section.

VII. CORRECTED $\langle k_T \rangle$ RESULTS

The $\hat{x}_h^{-1} \langle z_t \rangle \sqrt{\langle k_T^2 \rangle}$ extracted according to Eq. (22) for various p_{Tt} and p_{Ta} are shown in Fig. 16 and Fig. 17. In order to extract a $\sqrt{\langle k_T^2 \rangle}$ values we have solved

$$x_h^{-1} \sqrt{\langle p_{out}^2 \rangle} - \langle j_{Ty}^2 \rangle (x_h^2 + 1) - \hat{x}_h^{-1} \langle z_t \rangle \sqrt{\langle k_T^2 \rangle} = 0 \quad (49)$$

for $\sqrt{\langle k_T^2 \rangle}$ where the $\langle z_t \rangle$ and $\hat{x}_h = \langle \hat{p}_{Ta} \rangle / \langle \hat{p}_{Tt} \rangle$ are evaluated according Eq. (47) and Eq. (48) respectively. These two quantities depend on $\sqrt{\langle k_T^2 \rangle}$ so we solved Eq. (49) iteratively by varying a $\sqrt{\langle k_T^2 \rangle}$ value and in every step the $\langle z_t \rangle$ and \hat{x}_h were recalculated. To do so we need to know unsmeared final state parton spectrum $\Sigma_q(\hat{p}_T)$ and the fragmentation function. For the latter one we used the LEP data (see Fig. 22) where the fragmentation functions of gluon and quark jets were measured in e^+e^- collision at $\sqrt{s} = 180$ GeV. We have chosen

$$D_\pi^q \propto z^{-\alpha} (1-z)^\beta (1+z)^{-\gamma} \quad (50)$$

form used *e.g.* in [46] and extracted α , β and γ parameters from the fit to distributions shown in Fig. 22 (see Tab. VIII).

TABLE VIII: Extracted values of $D(z)$ parameters according Eq. (50) from the fit to the LEP data and power n of the unsmeared final state parton spectra $\Sigma_q(\hat{p}_T)$ extracted from the fit to the single inclusive π^0 invariant cross section [37] for corresponding fragmentation function and fixed value of $\sqrt{\langle k_T^2 \rangle} = 2.5$ GeV/c.

	gluon	quark	(gluon+quark)/2
α	0.16	0.49	0.32
β	0.88	0.57	0.72
γ	13.29	8.00	10.65
n	7.53	7.28	7.40

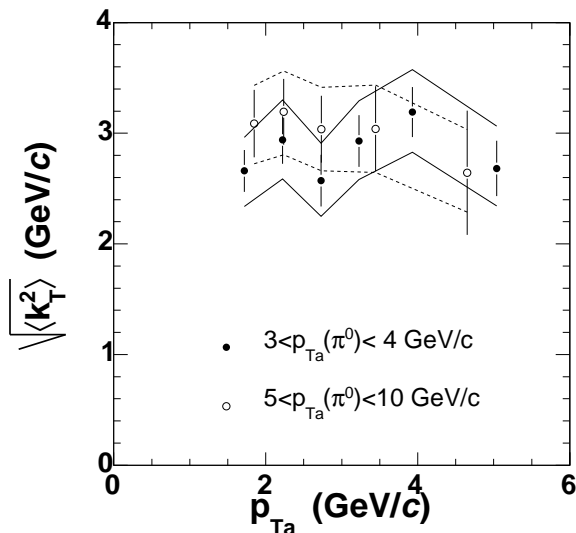


FIG. 26: $\sqrt{\langle k_T^2 \rangle}$ values corresponding to Fig. 16 as a solution to Eq. (49) for trigger π^0 in $3 < p_{Tt} < 4$ GeV/c (solid symbols) and $5 < p_{Tt} < 10$ GeV/c (open symbols) range. The solid and dashed lines bracket the systematic uncertainty due to the unknown ratio of quark and gluon jets, for the solid and open symbols, respectively.

For a given set of parameters α , β and γ the power of the unsmeared final state parton spectra $\Sigma_q(\hat{p}_T)$ was evaluated from the fit formula Eq. (27) to the single inclusive π^0 invariant cross section [37]. Here we used the simplified k_T smearing

$$f'_q(\hat{p}_{Tt}) = \frac{1}{\hat{p}_{Tt}} \Sigma'_q(\hat{p}_{Tt}) = \frac{1}{\hat{p}_T} \Sigma_q(\hat{p}_T) \otimes \exp \frac{-(\hat{p}_T - \hat{p}_{Tt})^2}{\langle k_{Tx}^2 \rangle}$$

and for the fixed value of $\sqrt{\langle k_T^2 \rangle} = \sqrt{2} \sqrt{\langle k_{Tx}^2 \rangle} = 2.5$ GeV/c the power n of $\Sigma_q(\hat{p}_T)$ distribution was determined.

The measurement of the fragmentation functions at LEP was done separately for quark and gluon jets and

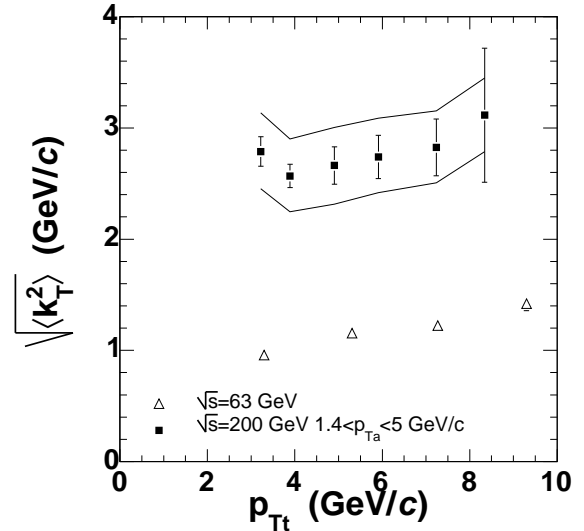


FIG. 27: $\sqrt{\langle k_T^2 \rangle}$ values corresponding to Fig. 17 as a solution to Eq. (49) for associated particles in $1.4 < p_{Ta} < 5$ GeV/c region (solid symbols). The solid lines bracket the systematic error due to the unknown ratio of quark and gluon jets. The CCOR measurement at $\sqrt{s}=62.4$ GeV [1] (empty triangles).

the slopes of these two $D(z)$ distributions are different. Quark jets produce a significantly harder spectrum than gluon jets (see Fig. 22). Since the relative abundance of quark and gluon jets at $\sqrt{s}=200$ GeV is not known, for the final results we assumed that the numbers of quark and gluon jets are equal; the final $D(z)$ uses the averaged parameter values between quark and gluon and the difference was used as a measure of the systematic uncertainty.

Resulting $\sqrt{\langle k_T^2 \rangle}$ values for $3 < p_{Tt} < 4$ GeV/c and $5 < p_{Tt} < 10$ GeV/c as a function of p_{Ta} are shown in Fig. 26 (compare to uncorrected values Fig. 17). The solid and dashed lines bracket the systematic error due to the unknown ratio of quark and gluon jets. These data points correspond to the uncorrected $\hat{x}_h^{-1} \langle z_t \rangle \sqrt{\langle k_T^2 \rangle}$ values shown in Fig. 16. The $\sqrt{\langle k_T^2 \rangle}$ values for varying p_{Tt} corresponding to the data shown of Fig. 17 are shown in Fig. 27. Also here the solid lines bracket the systematic error due to the unknown ratio of quark and gluon jets. It is evident that unfolded $\sqrt{\langle k_T^2 \rangle}$ values reveal, within the error bars, no dependence neither on p_{Ta} nor on p_{Tt} . The tabulated data are given in Table IX.

We compared the $\sqrt{\langle k_T^2 \rangle}$ data obtained in this analysis to $\sqrt{\langle k_T^2 \rangle}$ values found by the CCOR collaboration at $\sqrt{s}=62.4$ GeV [1] (empty triangles on Fig. 27). Although the trend with p_{Tt} seems to be similar the overall magnitude at $\sqrt{s}=200$ GeV is significantly higher.

The $\langle z_t \rangle$ and \hat{x}_h values from the iterative solution of Eq. (49) as a function of the π^0 trigger momenta p_{Tt} and associated momenta p_{Ta} are shown in Fig. 28 and

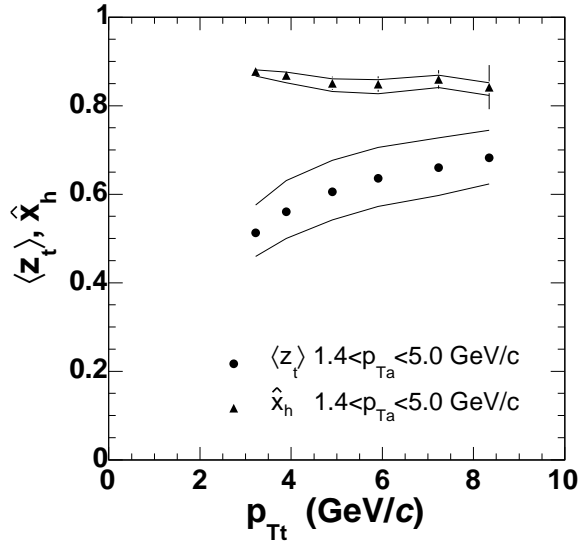


FIG. 28: $\langle z_t \rangle$ and \hat{x}_h as a function of p_{Tt} for the $1.4 < p_{Ta} < 5.0$ GeV/c associated region.

TABLE IX: Values of $\hat{x}_h^{-1} \langle z_t \rangle \sqrt{\langle k_T^2 \rangle}$ and $\sqrt{\langle k_T^2 \rangle}$ for various trigger particle p_{Tt} and associated momenta in the $1.4 < p_{Ta} < 5.0$ GeV/c region shown in Fig. 17 and Fig. 27

p_{Tt} GeV/c	$\hat{x}_h^{-1} \langle z_t \rangle \sqrt{\langle k_T^2 \rangle}$ GeV/c	$\sqrt{\langle k_T^2 \rangle}$ GeV/c
3.22	1.63 ± 0.08	$2.79 \pm 0.13 \pm 0.35$
3.89	1.66 ± 0.08	$2.57 \pm 0.11 \pm 0.33$
4.90	1.89 ± 0.13	$2.66 \pm 0.17 \pm 0.35$
5.91	2.06 ± 0.19	$2.74 \pm 0.20 \pm 0.34$
7.24	2.17 ± 0.25	$2.83 \pm 0.25 \pm 0.32$
8.34	2.53 ± 0.62	$3.11 \pm 0.60 \pm 0.33$

Fig. 29. There is an opposite trend; whereas the $\langle z_t \rangle$ rises with p_{Tt} it is falling with p_{Ta} . It is an interesting consequence of two effects: competition between steeply falling final state parton spectra and rising fragmentation function with parton momentum. Secondly, the detection of trigger particle biases the \vec{k}_T vector in the direction of the trigger jet as discussed in section VI B.

The p_{Tt} averaged value of $\sqrt{\langle k_T^2 \rangle}$ (Fig. 27) is compared to the average parton pair momentum, $\langle \hat{p}_n \rangle = \langle p_T \rangle_{pair}$, presented in [26] (see Fig. 30). The value of $\langle p_T \rangle_{pair}$ is determined as a sum of the two partons' k_T . In the present analysis the $\sqrt{\langle k_T^2 \rangle}$ is determined and thus the value of $\langle p_T \rangle_{pair}$ is evaluated as $\langle p_T \rangle_{pair} = \sqrt{2} \times \langle k_T \rangle = \sqrt{\pi/2} \times \sqrt{\langle k_T^2 \rangle}$.

The present value of $\langle p_T \rangle_{pair}$

$$\langle p_T \rangle_{pair} = 3.36 \pm 0.09(\text{stat}) \pm 0.43(\text{sys}) \text{ GeV/c}$$

appears to be in a good agreement with the lower energy dijet and dilepton measurements or the higher energy measurement in diphoton production [48]. A UA2 mea-

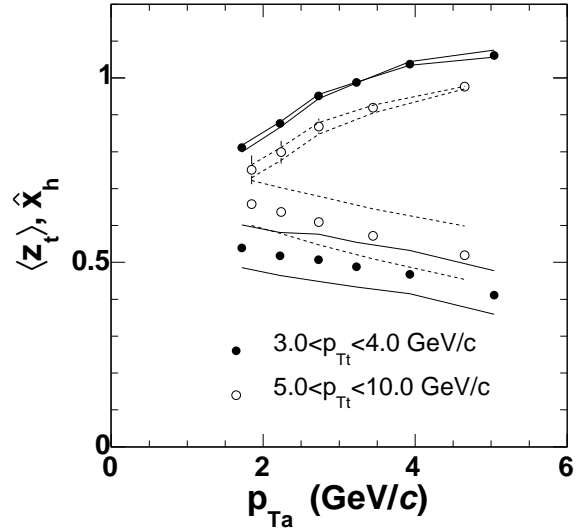


FIG. 29: The $\langle z_t \rangle$ and \hat{x}_h values (see Eq. 20) as solution of Eq. (48) for $3 < p_{Tt} < 4$ GeV/c and $5 < p_{Tt} < 10$ GeV/c as a function of p_{Ta} .

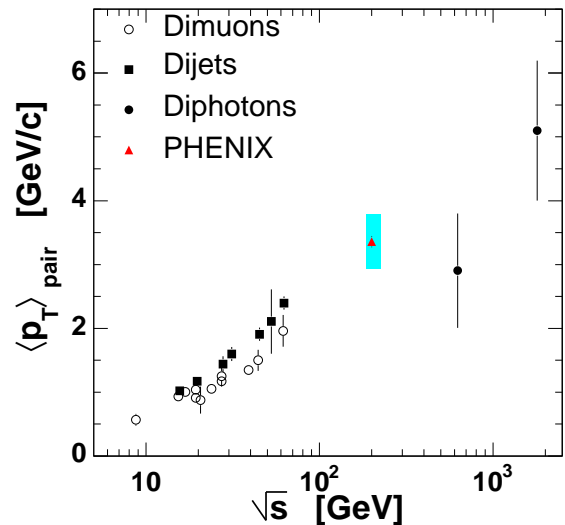


FIG. 30: (color online) Compilation of mean pair p_T measurements [26] and comparisons to the $\langle p_T \rangle_{pair}$ measured in this analysis.

surement of $\langle p_T \rangle$ of Z^0 production at $\sqrt{s} \sim 600$ GeV gives 8.6 ± 1.5 GeV/c [49, 50].

VIII. SUMMARY

We have made the first measurement of jet j_T and k_T for $p + p$ collisions at $\sqrt{s} = 200$ GeV using the method of two-particle correlations. Analysis of the

TABLE X: The $\hat{x}_h^{-1} \langle z_t \rangle \sqrt{\langle k_T^2 \rangle} \sqrt{\langle k_T^2 \rangle}$ values as a function of p_{T_a} for two different trigger π^0 transverse momentum bins shown in Fig. 16 and Fig. 26. All units in rad and GeV/c.

$3 < p_{T_t} < 4$			$5 < p_{T_t} < 10$		
p_{T_a}	$\frac{\langle z_t \rangle \sqrt{\langle k_T^2 \rangle}}{\hat{x}_h}$	$\sqrt{\langle k_T^2 \rangle}$	p_{T_a}	$\frac{\langle z_t \rangle \sqrt{\langle k_T^2 \rangle}}{\hat{x}_h}$	$\sqrt{\langle k_T^2 \rangle}$
1.7	1.76 ± 0.12	2.66 ± 0.19	1.9	2.69 ± 0.37	3.09 ± 0.30
2.2	1.74 ± 0.13	2.94 ± 0.22	2.2	2.54 ± 0.31	3.19 ± 0.30
2.7	1.37 ± 0.13	2.57 ± 0.23	2.7	2.13 ± 0.26	3.04 ± 0.30
3.2	1.45 ± 0.12	2.93 ± 0.23	3.4	1.89 ± 0.27	3.04 ± 0.38
3.9	1.44 ± 0.11	3.19 ± 0.23	4.7	1.41 ± 0.30	2.64 ± 0.56
5.0	1.04 ± 0.10	2.68 ± 0.25			

TABLE XI: The $\langle z_t \rangle$ and \hat{x}_h values with p_{T_t} shown in Fig. 28.

p_{T_t} (GeV/c)	$\langle z_t \rangle$	\hat{x}_h
3.22	$0.51 \pm 4.10^{-3} \pm 0.06$	0.88 ± 0.01
3.89	$0.56 \pm 2.10^{-3} \pm 0.07$	0.87 ± 0.01
4.90	$0.61 \pm 1.10^{-3} \pm 0.07$	0.85 ± 0.01
5.91	$0.64 \pm 1.10^{-4} \pm 0.07$	0.85 ± 0.02
7.24	$0.66 \pm 1.10^{-3} \pm 0.07$	0.86 ± 0.02
8.34	$0.68 \pm 5.10^{-3} \pm 0.06$	0.84 ± 0.05

TABLE XII: The $\langle z_t \rangle$ and \hat{x}_h values with p_{T_a} for two trigger π^0 momenta bins as shown on Fig. 29.

$3 < p_{T_t} < 4$ GeV/c		
p_{T_a}	$\langle z_t \rangle$	\hat{x}_h
1.72	$0.54 \pm 8.10^{-3} \pm 0.06$	0.81 ± 0.01
2.22	$0.52 \pm 6.10^{-3} \pm 0.06$	0.88 ± 0.01
2.73	$0.51 \pm 1.10^{-3} \pm 0.07$	0.95 ± 0.01
3.23	$0.49 \pm 1.10^{-3} \pm 0.06$	0.99 ± 0.01
3.93	$0.47 \pm 5.10^{-3} \pm 0.06$	1.04 ± 0.01
5.04	$0.41 \pm 6.10^{-3} \pm 0.06$	1.06 ± 0.01
$5 < p_{T_t} < 10$ GeV/c		
p_{T_a}	$\langle z_t \rangle$	\hat{x}_h
1.85	$0.66 \pm 4.10^{-3} \pm 0.06$	0.75 ± 0.04
2.24	$0.64 \pm 1.10^{-3} \pm 0.06$	0.80 ± 0.03
2.73	$0.61 \pm 2.10^{-3} \pm 0.07$	0.87 ± 0.02
3.44	$0.57 \pm 2.10^{-3} \pm 0.07$	0.92 ± 0.02
4.65	$0.52 \pm 5.10^{-3} \pm 0.08$	0.98 ± 0.01

angular widths of the near-side peak in the correlation function has determined that the jet fragmentation transverse momentum j_T is constant with trigger particle p_{T_t} and the extracted value $\sqrt{\langle j_T^2 \rangle} = 585 \pm 6(\text{stat}) \pm 15(\text{sys})$ MeV/c is comparable with previous lower \sqrt{s} measurements. The width of the away-side peak is shown to be a measure of the convolution of j_T with the jet momentum fraction z and the partonic transverse momentum k_T . $\langle z_t \rangle$ is determined through a combined analysis of the measured π^0 inclusive and associated spectra using the jet fragmentation functions from e^+e^- measurements. The average of $\langle z_t \rangle$ from the gluon and quark fragmentation functions is used and the difference is taken as the measure of the systematic

error. The final extracted values of k_T are then determined to be also independent of the transverse momentum of the trigger π^0 , in the range measured, with values of $\sqrt{\langle k_T^2 \rangle} = 2.68 \pm 0.07(\text{stat}) \pm 0.34(\text{sys})$ GeV/c.

Acknowledgments

We thank the staff of the Collider-Accelerator and Physics Departments at Brookhaven National Laboratory and the staff of the other PHENIX participating institutions for their vital contributions. We acknowledge support from the Department of Energy, Office of Science, Office of Nuclear Physics, the National Science Foundation, Abilene Christian University Research Council, Research Foundation of SUNY, and Dean of the College of Arts and Sciences, Vanderbilt University (U.S.A), Ministry of Education, Culture, Sports, Science, and Technology and the Japan Society for the Promotion of Science (Japan), Conselho Nacional de Desenvolvimento Científico e Tecnológico and Fundação de Amparo à Pesquisa do Estado de São Paulo (Brazil), Natural Science Foundation of China (People's Republic of China), Centre National de la Recherche Scientifique, Commissariat à l'Énergie Atomique, and Institut National de Physique Nucléaire et de Physique des Particules (France), Ministry of Industry, Science and Technologies, Bundesministerium für Bildung und Forschung, Deutscher Akademischer Austausch Dienst, and Alexander von Humboldt Stiftung (Germany), Hungarian National Science Fund, OTKA (Hungary), Department of Atomic Energy (India), Israel Science Foundation (Israel), Korea Research Foundation, Center for High Energy Physics, and Korea Science and Engineering Foundation (Korea), Ministry of Education and Science, Russia Academy of Sciences, Federal Agency of Atomic Energy (Russia), VR and the Wallenberg Foundation (Sweden), the U.S. Civilian Research and Development Foundation for the Independent States of the Former Soviet Union, the US-Hungarian NSF-OTKA-MTA, and the US-Israel Binational Science Foundation.

APPENDIX A

1. First and second moments of normally distributed quantities

Let x be a 1D variable with normal (Gaussian) distribution and $r = \sqrt{x^2 + y^2}$ is a 2D variable with x and y of normal distribution then the following relations can be easily derived

$\langle x \rangle$	=	0	$\langle r \rangle$	=	$\sqrt{\frac{\pi}{2}}\sigma_1$
$\langle x \rangle$	=	$\sqrt{\frac{2}{\pi}}\sigma_1$	$\langle r \rangle$	=	$\langle r \rangle$
$\langle x^2 \rangle$	=	σ_1^2	$\langle r^2 \rangle$	=	$2\sigma_1^2 \equiv \sigma_2^2$

Both \vec{j}_T and \vec{k}_T are two dimensional vectors. We assume Gaussian distributed x and y components and thus the mean value $\langle k_{Tx} \rangle$ and $\langle k_{Ty} \rangle$ is equal to zero. The non-zero moments of 2D Gaussian distribution are *e.g.* the root mean squares $\sqrt{\langle j_T^2 \rangle}$, $\sqrt{\langle k_T^2 \rangle}$ or the mean absolute values of the \vec{j}_T , \vec{k}_T projections into the perpendicular plane to the jet axes $\langle |j_{Ty}| \rangle$ and $\langle |k_{Ty}| \rangle$. Note that there are a trivial correspondences

$$\sqrt{\langle k_T^2 \rangle} = \frac{2}{\sqrt{\pi}} \langle k_T \rangle = \sqrt{\pi} \langle |k_{Ty}| \rangle \quad (\text{A1})$$

2. The correct way to analyze the azimuthal correlation function.

Construction and fitting of the two-particle azimuthal correlation function is discussed in section IV. Traditionally the correlation function is fitted by two Gaussian functions - one for intra-jet correlation (near peak) and one for the inter-jet correlations (away-side peak). From the extracted variances of the Gaussian functions the j_T and p_{out} magnitudes are extracted.

There is, however, a fundamental problem with this approach. The p_{out} -vector defined in Eq. (17) is equal to $p_{T_a} \sin \Delta\phi$ event by event. However, we measure the width of the correlation peak and this corresponds to $\sqrt{\langle \Delta\phi^2 \rangle} = \sigma_A$. The relation $\sqrt{\langle p_{\text{out}}^2 \rangle} \approx p_{T_a} \sin \sigma_A$ is not a good approximation for $\sigma_A > 0.4$ rad (see Fig. 31). The assumption that the away-side correlation has a Gaussian shape is also good only for small values of σ_A (see Fig. 31).

One way of relating $\sqrt{\langle p_{\text{out}}^2 \rangle}$ and σ_A was proposed *e.g.* by Peter Levai [42] and used in several other analyzes. Since $\sqrt{\langle p_{\text{out}}^2 \rangle} = p_{T_a} \sqrt{\langle \sin^2 \Delta\phi \rangle}$ one possibility how to relate p_{out} and σ_A is to expand

$$\begin{aligned} \langle \sin^2 \Delta\phi \rangle &= \left\langle \Delta\phi^2 - \frac{1}{3}\Delta\phi^4 + \frac{2}{45}\Delta\phi^6 \dots \right\rangle \\ &= \sigma_A^2 - \sigma_A^4 + \frac{2}{3}\sigma_A^6 \dots \end{aligned}$$

where we assumed a Gaussian distribution of $\Delta\phi$. The

comparison of $p_{T_a} \cdot (\sigma_A^2 - \sigma_A^4 + \frac{2}{3}\sigma_A^6 \dots)$ with the true p_{out} magnitude (simple monte carlo) for various σ_A

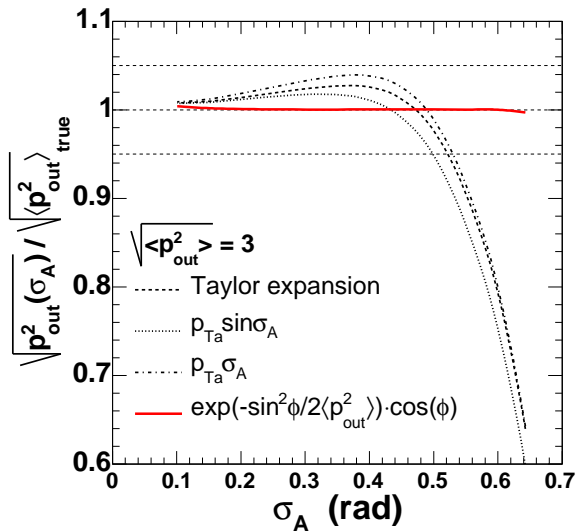


FIG. 31: (color online) The relative error on p_{out} determination from the azimuthal correlation function based on the Taylor expansion of $\langle \sin^2 \Delta\phi \rangle$ (dashed line), with an assumption of $\sqrt{\langle p_{\text{out}}^2 \rangle} = p_{T_a} \sin \sigma_A$ (dotted line) and $\sqrt{\langle p_{\text{out}}^2 \rangle} = p_{T_a} \sigma_A$ (dash-dotted line). The solid red line corresponds to $\sqrt{\langle p_{\text{out}}^2 \rangle}$ from Eq. (23).

values is shown in Fig. 31. It is obvious that there is only a little difference between $\sqrt{\langle p_{\text{out}}^2 \rangle} = p_{T_a} \sin \sigma_A$, $\sqrt{\langle p_{\text{out}}^2 \rangle} = p_{T_a} \sigma_A$ and the Taylor series. In the region where $\sigma_A > 0.4$ rad, all approximations seems to be equally bad.

However, p_{out} , the only quantity with a truly Gaussian distribution (if we neglect the radiative corrections responsible for non-Gaussian tails in the p_{out} distribution which are anyway not relevant for the k_T analysis) can be directly extracted from the correlation function. With the assumption of Gaussian distribution in p_{out} , we can write the away-side $\Delta\phi$ -distribution (normalized to unity) as

$$\begin{aligned} \frac{dN_{\text{away}}}{d\Delta\phi} \Big|_{\pi/2}^{3\pi/2} &= \frac{dN}{dp_{\text{out}}} \frac{dp_{\text{out}}}{d\Delta\phi} = \\ &= \frac{-p_{T_a} \cos \Delta\phi}{\sqrt{2\pi} \langle p_{\text{out}}^2 \rangle \text{Erf}\left(\frac{\sqrt{2}p_{T_a}}{\sqrt{\langle p_{\text{out}}^2 \rangle}}\right)} \exp\left(-\frac{p_{T_a}^2 \sin^2 \Delta\phi}{2 \langle p_{\text{out}}^2 \rangle}\right) \end{aligned}$$

This is the correct way of extracting a dimensional quantity from the azimuthal correlation function in the case of narrow associated bin. Similar line of arguments can be drawn also in the case of near peak. However, given the narrowness of the near angle peak, the simple Gaussian approximation is good enough.

-
- [1] A. L. S. Angelis et al. (CERN-Columbia-Oxford-Rockefeller), Phys. Lett. **B97**, 163 (1980).
- [2] P. Darriulat et al., Nucl. Phys. **B107**, 429 (1976).
- [3] M. Della Negra et al. (CERN-College de France-Heidelberg-Karlsruhe), Nucl. Phys. **B127**, 1 (1977).
- [4] K. Adcox et al. (PHENIX), Phys. Rev. Lett. **88**, 022301 (2002), nucl-ex/0109003.
- [5] S. S. Adler et al. (PHENIX), Phys. Rev. Lett. **91**, 072303 (2003), nucl-ex/0306021.
- [6] S. S. Adler et al. (PHENIX), Phys. Rev. Lett. **91**, 182301 (2003), nucl-ex/0305013.
- [7] C. Adler et al. (STAR), Phys. Rev. Lett. **90**, 032301 (2003), nucl-ex/0206006.
- [8] C. Adler et al. (STAR), Phys. Rev. Lett. **90**, 082302 (2003), nucl-ex/0210033.
- [9] A. B. Migdal, Phys. Rev. **103**, 1811 (1956).
- [10] X.-N. Wang and M. Gyulassy, Phys. Rev. Lett. **68**, 1480 (1992).
- [11] X.-N. Wang, Phys. Rev. **C58**, 2321 (1998), hep-ph/9804357.
- [12] C. A. Salgado and U. A. Wiedemann, Phys. Rev. Lett. **93**, 042301 (2004), hep-ph/0310079.
- [13] J.-w. Qiu and I. Vitev, Phys. Lett. **B570**, 161 (2003), nucl-th/0306039.
- [14] X.-N. Wang, Nucl. Phys. **A702**, 238 (2002), hep-ph/0208094.
- [15] S. M. Berman, J. D. Bjorken, and J. B. Kogut, Phys. Rev. **D4**, 3388 (1971).
- [16] J. F. Owens and J. D. Kimel, Phys. Rev. **D18**, 3313 (1978).
- [17] J. F. Owens, E. Reya, and M. Gluck, Phys. Rev. **D18**, 1501 (1978).
- [18] R. P. Feynman, R. D. Field, and G. C. Fox, Phys. Rev. **D18**, 3320 (1978).
- [19] J. F. Owens, Rev. Mod. Phys. **59**, 465 (1987).
- [20] G. Bunce, N. Saito, J. Soffer, and W. Vogelsang, Ann. Rev. Nucl. Part. Sci. **50**, 525 (2000), hep-ph/0007218.
- [21] R. Cutler and D. W. Sivers, Phys. Rev. **D17**, 196 (1978).
- [22] R. Cutler and D. W. Sivers, Phys. Rev. **D16**, 679 (1977).
- [23] B. L. Combridge, J. Kripfganz, and J. Ranft, Phys. Lett. **B70**, 234 (1977).
- [24] R. P. Feynman, R. D. Field, and G. C. Fox, Nucl. Phys. **B128**, 1 (1977).
- [25] Y. L. Dokshitzer, V. A. Khoze, A. H. Mueller, and S. I. Troian, *Basics of perturbative qcd*, gif-sur-Yvette, France: Ed. Frontieres (1991) 274 p. (Basics of).
- [26] L. Apanasevich et al., Phys. Rev. **D59**, 074007 (1999), hep-ph/9808467.
- [27] A. Kulesza, G. Sterman, and W. Vogelsang, Nucl. Phys. **A721**, 591 (2003), hep-ph/0302121.
- [28] F. W. Busser et al., Phys. Lett. **B46**, 471 (1973).
- [29] S. M. Berman, J. D. Bjorken, and J. B. Kogut, Phys. Rev. **D4**, 3388 (1971).
- [30] R. Blankenbecler, S. J. Brodsky, and J. F. Gunion, Phys. Lett. **B42**, 461 (1972).
- [31] D. Antreasyan et al., Phys. Rev. **D19**, 764 (1979).
- [32] P. Darriulat, Ann. Rev. Nucl. Part. Sci. **30**, 159 (1980).
- [33] K. Adachi et al. (TOPAZ), Phys. Lett. **B451**, 256 (1999), hep-ex/9901036.
- [34] K. Adcox et al. (PHENIX), Nucl. Instrum. Meth. **A499**, 469 (2003).
- [35] L. Aphecetche et al. (PHENIX), Nucl. Instrum. Meth. **A499**, 521 (2003).
- [36] K. Adcox et al. (PHENIX), Nucl. Instrum. Meth. **A499**, 489 (2003).
- [37] S. S. Adler et al. (PHENIX), Phys. Rev. Lett. **91**, 241803 (2003), hep-ex/0304038.
- [38] L. Aphecetche et al. (PHENIX), Nucl. Instrum. Meth. **A499**, 521 (2003).
- [39] M. Aizawa et al. (PHENIX), Nucl. Instrum. Meth. **A499**, 508 (2003).
- [40] S. S. Adler et al. (PHENIX), Phys. Rev. **C69**, 034910 (2004), nucl-ex/0308006.
- [41] S. S. Adler et al. (PHENIX), Phys. Rev. Lett. **94**, 082301 (2005), nucl-ex/0409028.
- [42] P. Levai, G. Fai, and G. Papp, *Dijet correlations at isr and rhic energies*, hep-ph/0502238.
- [43] J. Adams et al. (STAR), Phys. Rev. Lett. **91**, 072304 (2003), nucl-ex/0306024.
- [44] G. W. van Apeldoorn et al., Nucl. Phys. **B91**, 1 (1975).
- [45] X.-N. Wang, Phys. Lett. **B595**, 165 (2004), nucl-th/0305010.
- [46] P. Abreu et al. (DELPHI), Eur. Phys. J. **C13**, 573 (2000).
- [47] G. Alexander et al. (OPAL), Z. Phys. **C69**, 543 (1996).
- [48] F. Abe et al. (CDF), Phys. Rev. Lett. **70**, 2232 (1993).
- [49] R. Ansari et al. (UA2), Phys. Lett. **B194**, 158 (1987).
- [50] R. Ansari et al. (UA2), Z. Phys. **C41**, 395 (1988).

